PhD Dissertation

Doctorate School in Information and Communication Technology and Engineering

XXXVIII Cycle

Dipartimento di Ingegneria

Università degli Studi di Napoli "Parthenope"

Monitoring of Cryospheric and Hydrological Systems Using Polarimetric Synthetic Aperture Radar

Mozhgan Zahriban Hesari

Advisor: Prof. Maurizio Migliaccio

Coordinator: Prof. Agostino Iadicicco

2025/2026

Università degli Studi di Napoli "Parthenope"

Dipartimento di Ingegneria

Monitoring of Cryospheric and Hydrological Systems Using Polarimetric Synthetic Aperture Radar

Mozhgan Zahriban Hesari

A thesis submitted for the degree of

European Philosophiae Doctor (PhD)

in

Information and Communication Technology and Engineering

Advisor

Prof. Maurizio Migliaccio

Università degli Studi di Napoli "Parthenope", Napoli, Italy

Coordinator

Prof. Agostino Iadicicco

Università degli Studi di Napoli "Parthenope", Napoli, Italy

Dedicated to my family

Acknowledgements

The completion of this dissertation marks the culmination of a challenging yet profoundly rewarding journey. I am sincerely thankful to all those whose support, encouragement, and guidance made this achievement possible.

First and foremost, my heartfelt gratitude goes to my **father, mother, and brother**, who have always stood by me with unconditional love, patience, and dedication. Your support has been the foundation of my strength, and I owe you so much for your constant encouragement and for always believing in me. Thank you for being an example of love and sacrifice, which I carry with me every day.

I would like to sincerely thank **Prof. Maurizio Migliaccio**, who has been a precious guide and mentor to me. Even when our perspectives differed, our discussions were always enriching and helped me grow as a researcher. I am truly grateful to him for encouraging me to attend this PhD course and for the opportunity to work under his supervision. Thank you for believing in me and for teaching me so much, not only as a researcher but also as a person.

My heartfelt thanks also go to **Prof. Ferdinando Nunziata** and **Prof. Andrea Buono**, whose support, friendship, and encouragement have meant so much to me throughout this journey. They were not only mentors but also true friends, always ready to listen, to guide, and to motivate me during the most challenging moments. I am deeply grateful to them for inviting me to the University of Naples "Parthenope" and for giving me the chance to grow both professionally and personally. Their kindness, trust, and belief in me opened the door to a new world of science and discovery, for which I will always be thankful.

Special thanks go to **Prof. Giuseppe Aulicino** and **Dr. Mohammed Dabboor**, who served as colleagues and contributors to this thesis. Their constructive feedback, scientific insight, and constant support have been greatly appreciated.

I would also like to express my sincere gratitude to **Dr. Hossein Aghabbaei** for his warm hospitality during my stay at the University of Twente. His kindness and support made my time there both productive and truly enjoyable.

I would like to express my special thanks to **Adil** and **Giovanna**, my dearest friends, for always being by my side through the most difficult moments of this Ph.D. journey. Your friendship, encouragement, and constant presence meant more to me than words can express.

A heartfelt thank you also goes to my wonderful **labmates**, *Emanuele, Tingyu, Farah, Zakir, Manu, Luigi, Anna, Mario, Yuan, Giovanni, Sami, Wenyu and Ying Ying*, and to my **Iranian friends**, *Aida,Susan, Amin, Reza, Atena, Pegah, Mehrsa, Zahra*, whose kindness, laughter, and companionship made me feel at home, even far away from my beloved Iran.

Finally, I would like to thank **Prof. Agostino Iadicicco**, the coordinator of the Ph.D. program, and **Prof. Flavio Esposito** for their continuous support and guidance over these two years. I am especially grateful for their constant availability, sense of responsibility, and for always handling every issue and bureaucratic matter with great patience and care throughout my doctoral journey.

A few words to myself, Mozhgan (Moji).

To the one who never stopped believing in her dreams, even when the road was steep, the nights were long, and the finish line seemed impossibly far away.

To the one who faced every challenge with courage, who stumbled and stood up again, who learned to find light in moments of uncertainty and to turn every struggle into a lesson.

Every page of this thesis carries traces of your tears, your hope, your countless sleepless nights, and your unwavering determination, but also the spark of curiosity, the joy of discovery, and the quiet strength that kept you moving forward.

More than any title or recognition, what truly matters is the person you have become along the way, stronger, wiser, and more compassionate.

Thank you, **Moji**, for never giving up on yourself, for believing even when it was hard to believe, and for proving that with love, persistence, and faith in your own heart, even the most distant dreams can come true.

And remember, this is not the end of your story. Your journey has only just begun, and the world will still hear much more from you in the years to come. ♡

Abstract

This PhD dissertation presents the main scientific contributions toward the observation and analysis of cryospheric and hydrological environments using dual- and compact-polarimetry (CP) Synthetic Aperture Radar (SAR) data acquired by several operational satellite missions. The research combines both theoretical and experimental developments to produce a range of value-added outcomes, including the extraction of ice and water boundaries, classification of coastal and inland areas, assessment of glacier and iceberg dynamics, and improved interpretation of polarimetric scattering mechanisms.

The common rationale underlying all proposed methodologies is the model-based exploitation of polarimetric features and their physical relationship with surface scattering processes. Both dual- and compact-polarimetric configurations are investigated, demonstrating that, even when the information content is reduced compared with full-polarimetric SAR, reliable and robust analyses can still be achieved through appropriate electromagnetic modelling and polarimetric decomposition.

This work represents one of the first efforts to apply compact-polarimetric data from the RADARSAT Constellation Mission (RCM) to the monitoring of Arctic and sub-Arctic lakes, and to use multi-polarisation SAR for the observation of Antarctic ice features such as the Drygalski Ice Tongue (DIT) and C33 iceberg. Furthermore, the study introduces a systematic evaluation of how imaging geometry, particularly the incidence angle affects the polarimetric separability and stability of natural surfaces.

Overall, the findings show that integrating geometric and polarimetric parameters provides a precise, physically grounded approach for large-scale monitoring of cryospheric and hydrological boundaries.

Keywords: Synthetic Aperture Radar, Compact polarimetry, Cryosphere, Glacier monitoring

Contents

List of Figures

List of Tables

Chapter 1

Introduction

Antarctica is the fifth-largest continent on Earth, after Asia, Africa, North America, and South America. Despite its vast size, it has the smallest human population of all continents. Climatically, it is the coldest, driest, and windiest region on the planet, with extremely low humidity and temperature, and it is almost entirely covered by ice and snow [4]. Beyond these extremes, Antarctica plays a critical role in the global climate system. Nearly ninety percent of the world's ice and more than three-quarters of its freshwater resources are stored there [5]. The continent has a strong influence on ocean circulation, weather patterns, and global temperature regulation [6], while also providing scientists with unique opportunities to study coastal and marine environments.

The importance of these ecosystems, however, is not limited to environmental dimensions. Antarctica also holds economic significance because of its richness in minerals and valuable metals. Interest in these resources has raised discussion of potential exploitation in what is now regarded as a strategically important region [7]. At the same time, these fragile ecosystems have long faced a range of natural and human-induced threats. Over the past few decades, global warming has put growing pressure on Antarctica's fragile environment. Many glaciers, ice sheets, and icebergs have thinned or pulled back, which in turn has caused sea levels to rise and created new risks for marine life and biodiversity [8]. Climate change is still the main reason behind these changes, but human actions have also made the situation worse by adding to the damage in Antarctic regions [9]. Because of all this, careful planning and regular environmental monitoring are needed more than ever to protect these sensitive ecosystems.

Antarctica demonstrates the strong link between ice and climate in the Southern Hemisphere, whereas the Canadian Arctic and sub-Arctic offer a valuable view of how

environmental conditions are changing in the North. Looking at both regions together helps build a broader and more complete understanding of global climate change, as well as a clearer sense of the challenges that lie ahead [10]. Large lakes and river systems there undergo pronounced annual freeze-thaw cycles; as the ice forms and melts, shorelines shift, revealing wider hydrological and ecological changes [11]. Such conditions allow scientists to examine how freshwater systems respond to variations in temperature, ice cover and vegetation within landscapes that are both sensitive and dynamic.

The Canadian Arctic, which contains many marine-terminating glaciers, demonstrates substantial environmental transformation [12]. Ongoing glacier retreat and thinning indicate how Northern Hemisphere ice masses respond to atmospheric and oceanic warming. Compared with Antarctica, the Canadian Arctic and sub-Arctic emphasize the shared processes that connect polar and northern regions and shape the global climate system. To understand these fast-changing cryospheric environments, researchers need observation methods that can cover wide areas and remain reliable under harsh and unpredictable conditions.

Traditionally, monitoring of these areas has relied on instruments mounted on research vessels. Although these instruments provide accurate and valuable data, their use is limited by safety concerns, logistical constraints and high operating costs [13–15]. Hence, remote sensing technology offers a practical alternative for observing these remote environments, providing rapid data acquisition, wide spatial coverage and regular temporal sampling even under harsh conditions [16, 17].Optical remote sensing, however, is restricted by cloud cover and the lack of sunlight during polar winters. Microwave remote sensing overcomes these limitations because it operates independently of illumination and weather, allowing continuous day- and night-time observations [18]. Among microwave tools, over the past few decades, SAR, as an active microwave imaging system, has become a powerful tool for studying glaciers, icebergs, sea ice and freshwater systems across both Antarctica and the Canadian Arctic-sub-Arctic regions.

This dissertation examines the monitoring of the challenging environments of Antarctica and the Canadian Arctic-sub-Arctic using dual-pol SAR measurements acquired by multiple spaceborne satellite systems.

Polarimetric SAR (PolSAR) techniques enable the extraction of detailed information about the physical and geometric properties of surface targets through the use of multiple microwave polarisation channels [19]. This capability is particularly valuable in polar research because it allows discrimination between different ice types [20],

monitoring of glacier and iceberg evolution [21] and analysis of subsurface structure [22]. In this study, single- and dual-pol C-band data are used to derive scattering features from icebergs, glaciers and freshwater lakes. These features provide additional information that supports the following aims:

1. **Detection:** apply unsupervised detection approaches to extract surface and iceberg profiles, and evaluate whether dual-pol SAR data enhance iceberg–clutter contrast and boundary delineation compared with single-polarisation (single-pol) imagery.

2. **Change monitoring:** monitor iceberg drift, glacier flow dynamics, and temporal variations in surface morphology using multi-temporal SAR observations.

3. **Scattering analysis:** investigate the scattering behaviour of icebergs, glaciers, and lake surfaces through polarimetric parameters derived from covariance- and Stokes-based representations to identify dominant scattering mechanisms.

The remainder of this dissertation is organised as follows. Chapter 2 introduces the theoretical background of SAR and polarimetric techniques. Chapter 3 presents Antarctic case studies focused on monitoring glaciers and icebergs. Chapter 4 examines the Canadian Arctic and sub-Arctic regions, with emphasis on glacier dynamics and the monitoring of freshwater lakes. Finally, Chapter 5 summarises the principal findings, discusses their broader implications for climate and environmental monitoring, and outlines future directions for extending this research.

Chapter 2

Theoretical background

2.1 Introduction

This chapter presents the theoretical background that supports the analyses and methodologies described in Chapters 3 and 4.

All the experiments and processing strategies developed in this thesis rely on two fundamental pillars: the exploitation of SAR polarimetry measurements and the physical interpretation of the scattering mechanisms that govern natural surfaces in cryospheric and freshwater environments. Accordingly, the key theoretical aspects of SAR imaging principles and polarimetric representations are introduced here to support a clear understanding of the results discussed in the following chapters.

PolSAR is an advanced radar imaging technique that records the polarisation state of the backscattered electromagnetic wave. By analysing how radar signals interact with different targets, PolSAR provides valuable insight into the scattering mechanisms that characterise both natural and human-made environments. It is well known that SAR images are affected by speckle, a granular fluctuation arising from the coherent nature of radar imaging. Although speckle is often regarded as noise, when properly modelled it carries statistical information about the structure and roughness of the observed surface.

In SAR polarimetry, the second-order statistical description of the scene is obtained through ensemble (or spatial) averaging over locally homogeneous regions. In simpler terms, the covariance and coherency matrices show how the radar signal's strength and phase vary together. By averaging the data over small uniform areas, these matrices help smooth out random speckle noise while keeping the important physical details, such as surface roughness, differences in dielectric properties, and internal structure, that describe how the surface interacts with the radar signal [23, 24].

In this chapter, the emphasis is placed on the theoretical background of SAR and its polarimetric configurations, specifically, the dual- and CP architectures that are central to the analyses of cryospheric and hydrological systems.

2.2 SAR

SAR is an active microwave remote sensing technology used to monitor, analyse, and study geophysical parameters and Earth's surface features at any time of day and in almost all weather conditions. Because the system itself transmits microwave radiation and measures the reflected signal from the Earth's surface, its operation is independent of sunlight and atmospheric cloudiness, providing highly reliable data under a wide range of conditions.

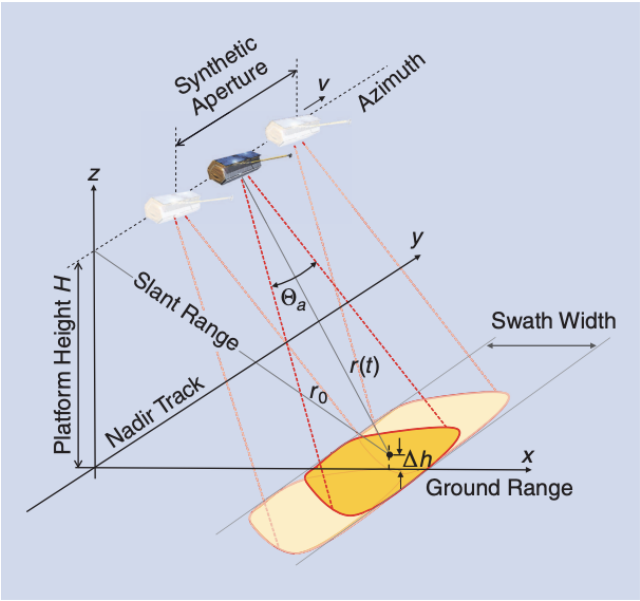

Figure 2.1 Illustration of the SAR imaging geometry. r_0 denotes the shortest approach distance, Θ_a the azimuth beamwidth, and v the sensor velocity. Source: [1].

SAR systems operate on the principle of the artificial aperture (or synthetic antenna), first proposed by Wiley [25]. According to this principle, a long antenna can be simulated by moving a short physical antenna along the flight path. The backscattered signals are recorded at successive positions and then coherently processed, using both the amplitude and phase of each echo, to obtain a reflection equivalent to that from a much longer antenna. This processing, now performed digitally, is the core of SAR image formation and greatly improves the azimuth (along-track) resolution. Owing to

this capability, SAR has become a key tool for monitoring and observing the Earth's surface [26] and even other planetary bodies [1].

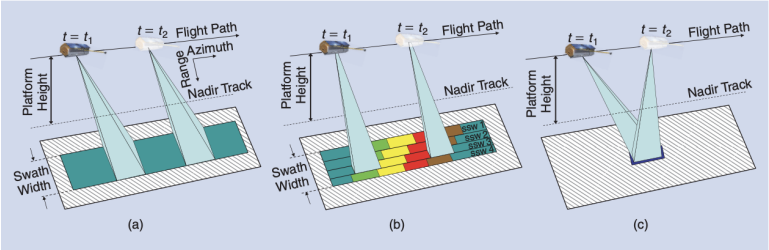

Figure 2.2 Common SAR imaging modes (Stripmap (a), ScanSAR (b) and, Spotlight (c)). Source: [1].

SAR systems can be operated in several imaging modes, depending on the balance between resolution and the area to be observed [1]. In the basic Stripmap mode, the antenna beam is fixed relative to the flight path, so that a continuous strip of the surface is imaged as the platform moves forward. In Spotlight mode, the beam is steered to keep the same ground target in view, improving azimuth resolution but reducing coverage area. The ScanSAR mode works differently: here, the beam switches between a number of adjacent swaths, allowing wider coverage but at the expense of resolution, since each section is observed for a shorter time. A common feature of all these modes is the side-looking geometry, where the radar antenna is oriented to the left or right of the flight path, approximately perpendicular to it, to minimise Doppler distortion and ensure uniform image coverage.

As a coherent imaging system, SAR is affected by the constructive and destructive interference of backscattered waves from numerous random scatterers within each resolution cell, producing a granular pattern known as speckle [27]. In SAR images, speckle shows up as a grainy variation in brightness from pixel to pixel. It is usually treated as a type of multiplicative noise that lowers the visual quality and radiometric reliability of the data. Yet, when examined carefully, speckle can also reveal useful statistical information about how rough or heterogeneous the surface is and how it scatters the radar signal [23, 24]. When properly modelled, it can be used to extract subpixel features, describe texture, and enhance classification and change-detection analyses. In addition, coherence between repeated SAR acquisitions forms the basis for interferometric and temporal analyses of surface dynamics.

Having reviewed the fundamental principles of SAR imaging, its operation, image formation, and the role of speckle, it is natural to ask what further insights can be derived from the coherent radar signal.This leads to the advanced field of SAR polarimetry. While a conventional SAR system records only one polarisation channel,

a PolSAR uses several combinations of transmit and receive polarisations. This allows a fuller description of how the radar signal interacts with the surface and reveals different scattering behaviours. By analysing how different surfaces interact with radar polarisation, PolSAR reveals details of the physical structure and dielectric properties of targets such as glaciers, snow, inland waters, vegetation, and human-made objects.

In the following section, the theoretical foundations of SAR polarimetry are presented, with emphasis on the dual-pol and CP configurations that form the basis of the analyses conducted in this thesis.

2.3 SAR Polarimetry

2.3.1 Foundations of Polarimetric SAR

PolSAR extends conventional radar imaging by capturing the polarisation state of the backscattered radar signal. By transmitting and receiving in different polarisation combinations, it yields detailed information about the scattering behaviour of both natural and human-made surfaces.

Under the backscattering alignment (BSA) convention and assuming reciprocity, the full-polarimetric scattering matrix $\mathbf{S}$ is defined as:

$$\mathbf{S} = \begin{pmatrix} S_{\mathrm{HH}} & S_{\mathrm{HV}} \\ S_{\mathrm{VH}} & S_{\mathrm{VV}} \end{pmatrix}, \tag{2.1}$$

where each complex element S_{pq}, with $p, q \in \{H, V\}$, represents the scattering amplitude corresponding to the transmit–receive polarisation pair. The $\mathbf{S}$ matrix therefore contains the complete polarimetric response of the target.

In most geophysical scenarios involving natural distributed targets, the reciprocity condition $S_{\mathrm{HV}} = S_{\mathrm{VH}}$ is a valid approximation, implying symmetry of the backscattering process with respect to the transmit/receive basis [28]. Accurate physical interpretation further relies on sound radiometric and polarimetric calibration to preserve amplitude balance and inter-channel phase integrity, ensuring that $\mathbf{S}$ represents the true target response across different sensors and viewing geometries [23].

From $\mathbf{S}$, second-order statistical descriptors can be derived, which are fundamental to the physical interpretation of SAR data.

The covariance matrix $\mathbf{C}$ and the coherency matrix $\mathbf{T}$ are Hermitian positive semi-definite matrices that describe the intensity and correlation properties of the scattering process.

These are related to $\mathbf{S}$ by ensemble averaging over homogeneous regions. An equivalent description in terms of the Stokes vector $\mathbf{s}$ and Mueller matrix $\mathbf{M}$ is often used, especially in CP, to represent the polarisation state of the scattered wave and its transformation through interaction with the target.

Physically, the backscattered radar signal results from the combination of three main scattering mechanisms:

- **Single-bounce (odd-bounce)** scattering: typical of smooth surfaces and Bragg-type reflections.
- **Double-bounce (even-bounce)** scattering: occurring between orthogonal surfaces, such as ice–water or building–ground interfaces.
- **Volume scattering**: produced by randomly oriented particles such as vegetation, snow, or broken ice.

2.3.2 Dual-pol SAR

In practice, fully polarimetric systems are costly and complex to operate, requiring the transmission and reception of both H and V polarisations. For many Earth observation missions, simplified architectures such as dual-pol SAR offer a good compromise between information content and resource efficiency [29, 30].

A dual-pol SAR measures coherently, i.e., both amplitude and inter-channel phase, either the first row of $\mathbf{S}$, $\mathbf{S}_{\mathrm{H}} = (S_{\mathrm{HH}}, S_{\mathrm{HV}})$, or the second row, $\mathbf{S}_{\mathrm{V}} = (S_{\mathrm{VH}}, S_{\mathrm{VV}})$. Although these modes provide only a partial characterisation of the scattering process, they have demonstrated significant value across cryospheric, hydrological, and oceanographic applications [21, 31, 32]. Information extraction from dual-pol data typically relies on quantities derived from the normalised radar cross-section (NRCS) of the two available channels, σ^0_{pp} and σ^0_{pq}, or from their complex correlation coefficient:

$$r = \langle S_{pp}\, {S_{pq}}^* \rangle, \tag{2.2}$$

where $\langle\cdot\rangle$ denotes spatial averaging and $(\cdot)^*$ the complex conjugate.

Beyond intensity-based metrics, polarimetric target decomposition techniques, originally developed for full-pol data, have been adapted to dual-pol configurations [28]. These are based on the covariance matrix, which for a horizontally transmitted mode reads:

$$\mathbf{C}_{\mathrm{H}} = \langle \mathbf{S}_{\mathrm{H}}\, \mathbf{S}_{\mathrm{H}}^{\dagger} \rangle,$$

where $(\cdot)^\dagger$ denotes the complex-conjugate transpose. This Hermitian matrix captures the joint statistics of the HH and HV channels and provides the foundation for several dual-pol descriptors.

Derived Polarimetric Features

From $\mathbf{C}_\mathrm{H}$, three principal observables are considered in this thesis to describe the C33 iceberg and its surroundings: σ^0_HH, σ^0_HV, and the co–cross-polarised correlation:

$$r_\mathrm{HV} = \langle |S_\mathrm{HH}| \cdot |S_\mathrm{HV}| \rangle. \tag{2.3}$$

To infer the scattering characteristics, the covariance matrix is decomposed into its eigencomponents:

$$\mathbf{C}_\mathrm{H} = \mathbf{U} \cdot \mathbf{D} \cdot \mathbf{U}^\dagger, \quad \lambda_1 \geq \lambda_2 \geq 0, \tag{2.4}$$

where $\mathbf{U}$ contains the eigenvectors and $\mathbf{D}$ is diagonal with eigenvalues λ_1 and λ_2. The power distribution between these eigenvalues reflects the degree of depolarisation, which is quantified by the degree of polarisation (DoP) [33]:

$$\mathrm{DoP} = \frac{\lambda_1 - \lambda_2}{\lambda_1 + \lambda_2}. \tag{2.5}$$

High DoP values are typically associated with deterministic scattering mechanisms such as surface or double-bounce reflections. In contrast, low DoP values indicate increased depolarisation arising from multiple scattering events within heterogeneous media. It is important to note that volumetric scattering is primarily controlled by internal structural complexity and layering rather than solely by apparent surface roughness at optical scales.

2.3.3 CP

CP is a dual-pol SAR imaging mode that, while preserving some of the key benefits typical of conventional dual-pol imaging modes as large swath width and limited transmitted power, is characterized by polarimetric performance which, for several applications, tend to the optimal case of a quad-polarimetric SAR imaging mode [34] and [35]. A CP SAR imaging mode is such that circularly or slant linearly polarized electromagnetic wave is transmitted while the backscattered wave is coherently received onto a conventional linearly polarized orthogonal basis, i. e., H-V [36]. Such imaging system is known as hybrid-polarimetric (HP) mode, while the latter is known as $\pi/4$ [35]. Some first attempts have been developed to implement the HP imaging mode as

Risat-1, Alos PalSAR-2. The RADARSAT Constellation Mission (RCM) is the most recent. When considering the HP mode, the backscattered electric field can be written as:

$$\mathbf{E}_r = \begin{pmatrix} E_{hq} \\ E_{vq} \end{pmatrix}, \tag{2.6}$$

where q stands for the transmitted polarization that can be a right-/left-handed circular. Circularly polarized electromagnetic waves, being rotationally invariant, result in polarimetric parameters which are invariant with respect to the geometric orientation of the observed scene and more robust to Faraday rotation effects [37]. From Eq. 2.6, the intensity associated to the two orthogonal components received at the HP SAR antenna once the transmitted wave is scattered off the target can be defined:

$$RH = |E_{RH}|^2, RV = |E_{RV}|^2 \tag{2.7}$$

where R stands for a right-hand circular transmitted polarization. When dealing with extended random targets, second-order descriptors are needed to fully characterize the polarization properties of the received electromagnetic wave. To this aim, wave polarization theory must be adopted that leads to either the 2×2 complex-valued coherence matrix Γ or the 4× 1 real-value Stokes vector:

$$\mathbf{\Gamma} = \langle \mathbf{E}_r \mathbf{E}_r^{\dagger} \rangle = \begin{pmatrix} \langle E_{hq} E_{hq}^* \rangle & \langle E_{hq} E_{vq}^* \rangle \\ \langle E_{vq} E_{hq}^* \rangle & \langle E_{vq} E_{vq}^* \rangle \end{pmatrix} = \begin{pmatrix} \Gamma_{hh} & \Gamma_{hv} \\ \Gamma_{vh} & \Gamma_{vv} \end{pmatrix}. \tag{2.8}$$

$$\mathbf{s} = \begin{pmatrix} \langle |E_{hq}|^2 + |E_{vq}|^2 \rangle \\ \langle |E_{hq}|^2 - |E_{vq}|^2 \rangle \\ 2\Re\left(\langle E_{hq} E_{vq}^* \rangle\right) \\ -2\Im\left(\langle E_{hq} E_{vq}^* \rangle\right) \end{pmatrix}^T, \quad s_0^2 \geq \sum_{i=1}^{3} s_i^2. \tag{2.9}$$

Once the scattered electromagnetic wave received under a HP SAR imaging mode is characterised, useful parameters can be equivalently derived from the coherence matrix $\mathbf{\Gamma}$ (see Eq. 2.8) or from the Stokes vector (see Eq. 2.9).

The wave degree of polarisation, denoted by m, represents the wave-based degree of polarisation derived from the Stokes formalism [38]. In this thesis, the symbol m is adopted for CP/HP data to distinguish it from the DoP previously defined for dual-pol covariance-based descriptors.

$$m = \sqrt{1 - \frac{4\det(\Gamma)}{\mathrm{tr}(\Gamma)^2}} = \frac{1}{s_0}\sqrt{\sum_{i=1}^{3} s_i^2}. \tag{2.10}$$

where $\mathrm{tr}(\cdot)$ and $\det((\cdot))$ operators stand for trace and determinant of the matrix. The parameter m is bounded in the range [0, 1], where values close to 0 characterize completely unpolarised electromagnetic waves, while values close to 1 are associated with fully polarised waves.

Hence, the received wave backscattered off the water surface is expected to call for large m values due to the dominant Bragg/tilted-Bragg scattering mechanism, while this is no longer the case of complex coastal scenarios where a combination of odd- and even-bounce and volume scattering may be in place resulting in a backscattered wave whose m value is smaller. The ellipticity parameter (EP) is an angle that lies in the range [–45°, +45°] and characterizes the polarization state of the backscattered wave in the polarization plane.

$$EP = -\frac{s_3}{m s_0}, \tag{2.11}$$

The EP values equal to ±45° refer to a left-/right-hand circular polarization, while EP = 0, means linear polarization. Accordingly, the sign of EP is related to the presence of odd- versus even-bounce backscattering, even when the transmitted field is not perfectly circularly polarized and, therefore, it can be used as an indicator of the presence of a dominant Bragg scattering [39]. Hence, the water surface is expected to call for negative EP values since Bragg scattering is a single-reflection mechanism, while mostly positive EP values are expected over coastal areas where a more randomness scattering process may occur due to the mixture of single- and double-bounce scattering mechanisms and volume scattering.

In this work, a Stokes-based version of the EP, denoted as EP_{ST}, is also used to maintain consistency with RCM HP data products. It is mathematically equivalent to Eq. 2.11, but expressed directly in terms of the normalised Stokes components:

$$EP_{ST} = -\frac{s_3}{\sqrt{s_1^2 + s_2^2 + s_3^2}}. \tag{2.12}$$

This form allows easier implementation in data-processing workflows where the Stokes parameters are provided in calibrated units.

The parameters m and EP_{ST} will be employed in the subsequent chapters as diagnostic indicators of dominant scattering regimes. In particular, their joint inter-

pretation helps discriminate Bragg-dominated open-water returns from more complex shoreline and mixed media responses, providing continuity between the theoretical constructs presented here and the practical analyses developed in Chapters 3 and 4.

Summary

This chapter outlined the physical and mathematical foundations of SAR and its polarimetric extensions with emphasis on dual-pol and CP configurations that balance information content and acquisition efficiency for wide-area monitoring. These principles underpin the detection, change-analysis, and scattering characterisation methodologies applied in the Antarctic and Canadian case studies presented in the following chapters.

Chapter 3

Antarctic Environment

3.1 Introduction

This chapter presents the main experimental results obtained from single and dual-pol SAR observations, focusing on their application to monitoring Antarctic glaciers and icebergs. In line with the research objectives introduced in Chapter 1, the study addresses three primary goals.

The first objective is to evaluate the capability of C-band SAR data to delineate ice boundaries under the challenging environmental conditions of the Drygalski Ice Tongue (DIT) region in Antarctica. For this purpose, two case studies were selected: the continental ice feature of the DIT itself, and the C33 iceberg located in Terra Nova Bay. Both single- and dual-pol Sentinel-1 C-band SAR datasets were employed, and several polarimetric features were analysed to enhance discrimination between ice and the surrounding ocean or sea-ice cover.

The second objective is to investigate the short- and long-term variability of the DIT and C33 iceberg by analysing their temporal evolution using time series of Sentinel-1 C-band SAR imagery. This analysis provides a quantitative assessment of spatiotemporal dynamics, including displacement, drift velocity, and rotational motion.

Finally, the third objective is to explore how the scattering properties of the C33 iceberg evolved as it drifted through Terra Nova Bay. This part of the study concentrates on polarimetric parameters derived from the covariance matrix, giving special attention to phase-based quantities such as the DoP. These metrics help interpret the dominant scattering behaviour and provide insight into the physical evolution of the iceberg over time.

This chapter includes two separate case studies, each based on previously published work. The first concerns the DIT, and the second concerns the C33 iceberg. Since the

two papers followed slightly different structures, they are presented here in their original form. In particular, the DIT section includes a separate methodology section, whereas in the C33 study, the methodological details are included within the experimental results.

3.2 DIT monitoring

3.2.1 Study area

The DIT is one of the largest ice tongues in Antarctica [40], located in East Antarctica between latitude 75°24′S and longitude 163°30′E of Victoria Land, and it extends up to the Ross Sea, see the red box in Figure 3.1. The DIT is 140 km long and 20 km wide and consists of a relatively stable ice sheet that terminates in the Ross Sea with a 90 km floating ice slab fed by the David Glacier, which flows through the Transantarctic Mountains between Mount Neumayer and Hughes Bluff [41]. From a historical viewpoint, DIT is at least 4,000 years old and during this time at least three significant calving events occurred. The first calving took place in the early 1900s [42]; the second one between 1956 and 1957 [41] when about 40 km of ice were lost from the end of the tongue. Finally, the last calving took place between 2005 and 2006 [43, 44], when about 300 km^2 of ice were calved off.

3.2.2 SAR datasets

The satellite data set consists of SAR imagery acquired by the Copernicus Earth observation Sentinel-1 mission, managed by the European Space Agency (ESA). The Sentinel-1 constellation initially comprised two polar-orbiting satellites equipped with identical C-band (5.405 GHz) SAR sensors, namely Sentinel-1A and Sentinel-1B. Following the loss of Sentinel-1B in 2022, the constellation is currently complemented by Sentinel-1C, which is in orbit and progressively ensuring mission continuity. The SAR instrument onboard Sentinel-1 supports single- and dual-polarimetric imaging capabilities and operates under four acquisition modes: Stripmap (SM), Extra-Wide Swath (EW), Wave (WV), and Interferometric Wide Swath (IW). The IW mode implements the Terrain Observation by Progressive Scans (TOPS) technique, producing three sub-swaths covering approximately 250 km in total width. This configuration spans an incidence angle range from about 30° to 46°, with a spatial resolution of approximately 5 m × 20 m. In this study, 18 Sentinel-1 SAR scenes acquired in IW mode between 2016 and 2021 are used (see Table 3.1). The short-term data set

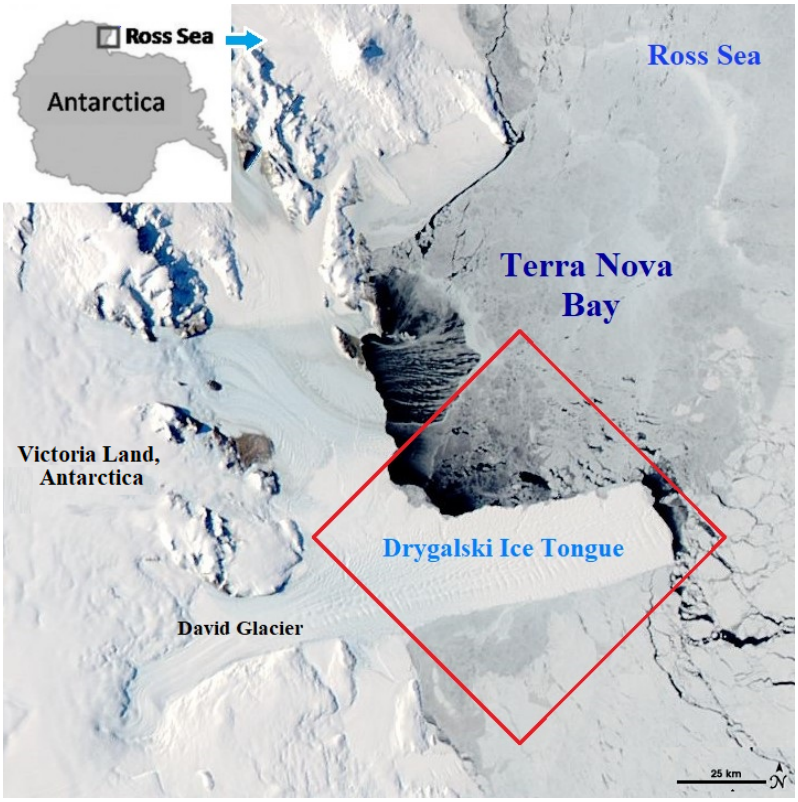

Figure 3.1 Moderate Resolution Imaging Spectroradiometer (MODIS) image collected over the Terra Nova Bay area on 16 October 2007 (adapted from [2]). DIT is enclosed in the red box.

(STDS) consists of six SAR scenes collected in descending orbit during April 2017. The long-term data set is constructed using one SAR acquisition per year, collected in ascending orbit from 2016 to 2021. To assess seasonal variability, the long-term analysis is further subdivided into March data set (MDS), referring to imagery acquired in March, and April data set (ADS), referring to imagery acquired in April.

3.2.3 Methodology

This section describes the methodology adopted to extract the DIT profile and to analyse its time variability. A flowchart of the processing chain is depicted in Figure 3.2, which consists of three key steps based on the methodology proposed in [45] to extract sandy and rocky coastlines from X-band SAR imagery. This methodology is here specialised to deal with the peculiarities of the clutter that consists of either ice-free or ice-infested seawater.

As introduced in Chapter 2, the analysis for the DIT case study was performed using the co-polarised backscattering channel (σ^0_{HH}), which provides higher contrast

Table 3.1 Summary of the Sentinel-1 SAR dataset used for the DIT analysis.

Time scale	Dataset label	Acquisition date	Polarisation
Short-term (STDS)		10 Apr 2017	HH+HV
		13 Apr 2017	HH+HV
		15 Apr 2017	HH+HV
		22 Apr 2017	HH+HV
		25 Apr 2017	HH+HV
		27 Apr 2017	HH+HV
Long-term (MDS)		21 Mar 2016	HH+HV
		16 Mar 2017	HH
		11 Mar 2018	HH
		18 Mar 2019	HH
		12 Mar 2020	HH
		19 Mar 2021	HH
Long-term (ADS)		14 Apr 2016	HH+HV
		09 Apr 2017	HH
		16 Apr 2018	HH
		11 Apr 2019	HH
		17 Apr 2020	HH
		12 Apr 2021	HH

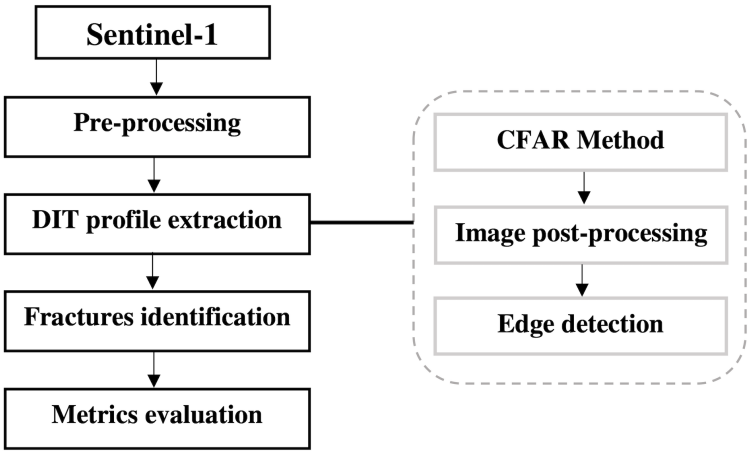

Figure 3.2 Flowchart of the proposed methodology.

between the ice surface and the surrounding ocean under C-band illumination. This choice ensures radiometric stability and enhances the separability between glaciated and non-glaciated areas.

The first step consists of pre-processing the SAR scene by applying radiometric calibration, speckle filtering using a 7×7 boxcar filter, and range–Doppler terrain correction using the Advanced Spaceborne Thermal Emission and Reflection Radiometer Digital Elevation Model (ASTER DEM). As a result, a pixel spacing of 14.4 m is obtained. A sample image belonging to the ADS together with intermediate outputs stemming from the processing chain are shown in Figure 3.3. The pre-processed HH-polarised SAR scene collected on 9 April 2017 is depicted (in decibel – dB – scale) in Figure 3.3(a).

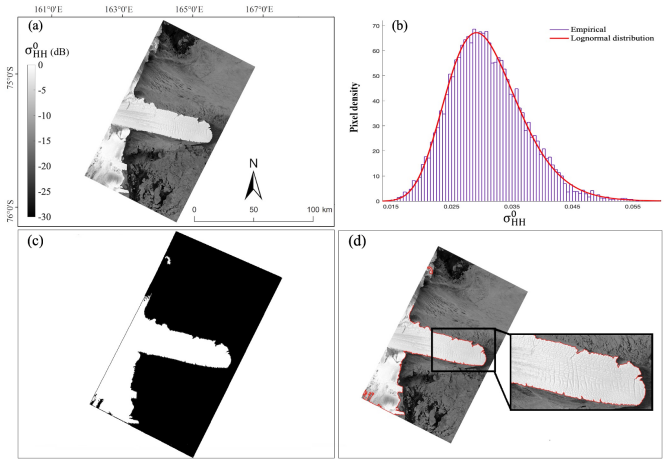

Figure 3.3 HH-polarised SAR scene collected on 9 April 2017. (a) Excerpt of the pre-processed SAR scene; (b) empirical PDF of the clutter where the theoretical lognormal distribution is also annotated in red; (c) binary image obtained using the CFAR method; (d) extracted coastline superimposed as a red line on the HH-polarised SAR scene. An enlarged version of the DIT area enclosed in the black rectangle is also annotated where fractures are visible.

The second step is to extract the DIT profile using a state-of-the-art global threshold constant false alarm rate (CFAR) method [45]. The CFAR approach has been extensively used to extract the coastline from SAR imagery with an exponentially distributed sea clutter. In this case, ice-free and ice-infested sea surface clutter distribution was found to be better approximated by a lognormal model, see Figure 3.3 (b), where the empirical distribution (in blue) is contrasted with the theoretical lognormal one (in red) to show that a good visual agreement applies. Note that, in all the experiments, the ability of the lognormal distribution to well approximate the actual clutter distribution is verified using the Kolmogorov–Smirnov goodness-of-fit test. Modeling the clutter distribution using a lognormal probability density function (PDF) provides a closed-form relationship between the global threshold t and the

probability of false alarm P_{fa} [46]:

$$P_{\text{fa}} = \int_t^{\infty} \frac{1}{x\,\sigma\sqrt{2\pi}} \exp\left[-\frac{(\ln x - \mu)^2}{2\sigma^2}\right] \mathrm{d}x = \frac{1}{2}\,\mathrm{erfc}\left(\frac{\ln t - \mu}{\sqrt{2}\sigma}\right) \tag{3.1}$$

where x is the HH-polarised SAR image pixel value, while σ, $\mathrm{erf}(\cdot)$ and t are the standard deviation (scale parameter) of the lognormal distribution, the error function and the threshold to be obtained, respectively. In this study, P_{fa} is empirically set to 10^{-6}. The CFAR output consists of a binary image where DIT is clearly distinguished from the clutter, see Figure 3.3 (c). Since this binary image may sometimes present some isolated false edges at sea, they are sorted out by conventional image processing tools, i. e.; morphological filters. Nonetheless, it is worth noting that these false edges do not belong to the area that surrounds the DIT, i. e., they do not affect the extraction results. Once the refined binary image is available, the actual DIT continuous profile is extracted using the optimal Canny edge detector that is based on a two-dimensional Gaussian kernel [47]. The DIT profile extracted from the binary image, superimposed as a red line on the pre-processed HH-polarised SAR scene, in shown in Figure 3.3 (d).

The third step consists of selecting some Region Of Interests (ROIs) on the extracted DIT profile to analyse the time variability of some meaningful features along the whole SAR data set. The following DIT features are considered: the ice front and the four most prominent fractures, i. e., the most visible ones. It has already been documented that the occurrence of fractures in DIT is due to its swings horizontally [48]. Also, storm events and iceberg collisions increase the horizontal motion of the ice tongue and the number of fractures[41, 44].

Two metrics are selected to quantitatively assess the DIT variability: the displacement of the reference features and the average surface velocity. The former metric is evaluated by measuring the distance between peer points identified on the extracted DIT profiles along the flow line and belonging to two consecutive years. Although it is true that the measured distance is point-dependent, we expect that the time variability of DIT inferred by this approach is, anyway, informative. The latter metric is estimated, for each feature, by averaging over years the total displacement.

3.2.4 Experimental results

In this section, experimental results are presented and discussed. First, the DIT extraction methodology is presented and the accuracy of the extracted profiles is discussed. Then, the time variability of the extracted DIT profile is analysed using the

STDS, MDS and ADS. Finally, the outcomes of this study are discussed with respect to the pertinent state-of-the-art.

Preliminary assessment

The first experiment is to show the ability of the proposed method to accurately extract the DIT profile. A thought example is presented that consists of processing the Sentinel-1 SAR scene collected on 9 April 2017. The output is depicted as a red line superimposed on the pre-processed HH-polarised SAR image, see Figure 3.3 (d), where a good visual agreement between the extracted boundary and the DIT profile is observed. The accuracy of the results can be better appreciated in the enlarged version of the seaward part of the DIT as highlighted in the inset of Figure 3.3 (d). This proves the ability of the proposed method to fit well the DIT profile and to identify its fractures. To qualitatively assess the accuracy of the extracted DIT profile, the latter is superimposed on the closest almost cloud-free Sentinel-2 optical image that covers the study area. Hence, the DIT profile extracted from the Sentinel-1 SAR image collected on 21 March 2016 is superimposed on the Sentinel-2 optical image (band 2, blue) on 19 March 2016, see Figure 3.4 (a); while the profile extracted from the Sentinel-1 SAR image collected on 19 March 2021 is contrasted with the Sentinel-2 optical image collected on 2 March 2021, see Figure 3.4 (b). In both cases, there is a remarkable agreement between the extracted DIT profile and the visually inspected from the optical image. The fractures/rifts well fit the features visually inspected from the optical imagery showing that the proposed methodology results in a good extraction accuracy.

Short-term analysis

The second experiment is to analyse the short-term DIT variability. The DIT profiles extracted using the STDS, see Table 3.1, are depicted in Figure 3.5, where the six profiles that belong to the six SAR scenes sampled in April 2017 are depicted using different colors. By visually inspecting the images, the six profiles appear very overlapped. This is also witnessed by the enlarged version of some ROIs that belong to the extracted profiles, see insets in Figure 3.5. The latter show that all the profiles are almost overlapped with an average separation among consecutive profiles being lower than 30 m (i. e., around 2 pixels according to the pixel spacing used in this study). Considering the ground-range pixel spacing (approximately 14 m) and the intrinsic uncertainty associated with the boundary extraction procedure, estimated to be within 1–2 pixels, the observed average separation (30 m) falls within the expected positional accuracy

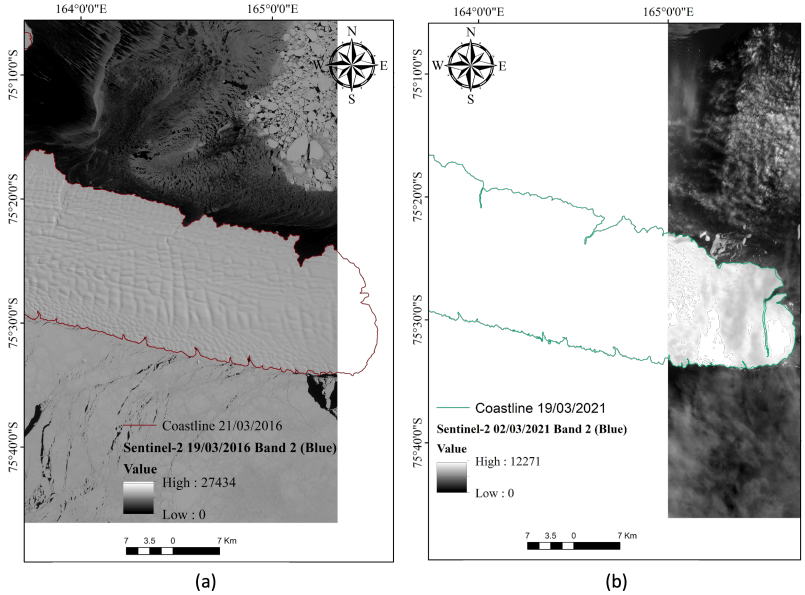

Figure 3.4 Preliminary assessment. (a) DIT profile extracted on 21 March 2016 overlaid (in red) on a reference Sentinel-2 optical image (band 2, blue) collected on 19 March 2016; (b) DIT profile extracted on 19 March 2021 overlaid (in green) on a reference Sentinel-2 optical image (band 2, blue) collected on 2 March 2021.

of the method. Therefore, the minor profile fluctuations observed in the STDS are not interpreted as true morphological changes but rather as extraction uncertainty and SAR imaging variability.

Table 3.2 Average surface velocity estimated for selected DIT features from the MDS and ADS datasets.

Feature	**MDS velocity ($\mathrm{m\,yr^{-1}}$)**	**ADS velocity ($\mathrm{m\,yr^{-1}}$)**
Ice front	675	667
Fracture 2	663	666
Fracture 3	614	619

Long-term analysis

The third experiment is to analyse the long-term variability using the MDS and ADS, see Table 3.2. An excerpt of the SAR scenes referred to the MDS and ADS is shown in Figure 3.6 and 3.7. The imagery shows the extracted DIT profiles as a red line superimposed onto the pre-processed HH-polarised SAR image. In both data sets, the presence of some fractures along the northern and southern sides of DIT can be observed, with the former being the biggest. Four fractures are selected along the

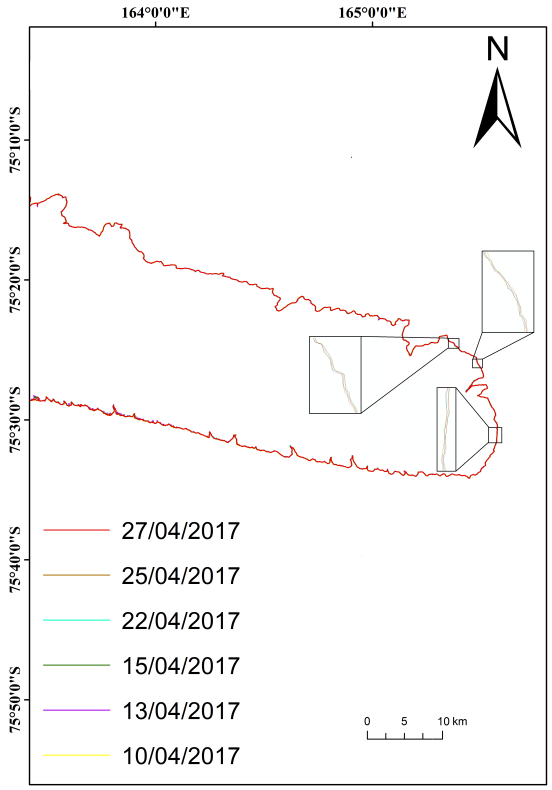

Figure 3.5 Short-term analysis performed on the STDS. The DIT profiles referred to six sample images collected on April 2017 are depicted using different colors. Selected ROIs, enclosed in the black boxes, are enlarged in the annotated insets.

northern part of the extracted profile to analyse the DIT time variability. They are labeled from "1" to "4" and highlighted in the extracted profile using yellow, blue, green and orange colors, respectively. The shape of most of the fractures changes over time. This is the case, for example, of the fracture labeled as "1" (highlighted in yellow), that moved southward, and the fracture labeled as "4" (highlighted in orange), that appeared for the first time in 2019. However, by visually contrasting imagery belonging to the MDS and ADS, no remarkable difference can be appreciated.

To provide a deeper analysis of the long-term variability of the DIT, its profiles extracted from the whole SAR data set are shown in Figure 3.8 where (a) and (b) refer to MDS and ADS, respectively. In Figure 3.8, different colors refer to the DIT profile extracted in different years, i. e., the profiles extracted in 2016, 2017, 2018, 2019, 2020 and 2021 are marked with red, green, purple, blue, yellow and black. The selected features, i. e., the ice front and the four fractures identified along the northern side, are also highlighted in the black insets to show how the displacement analysis is performed. Figure 3.8 clearly shows that, from 2016 to 2021, both the fractures

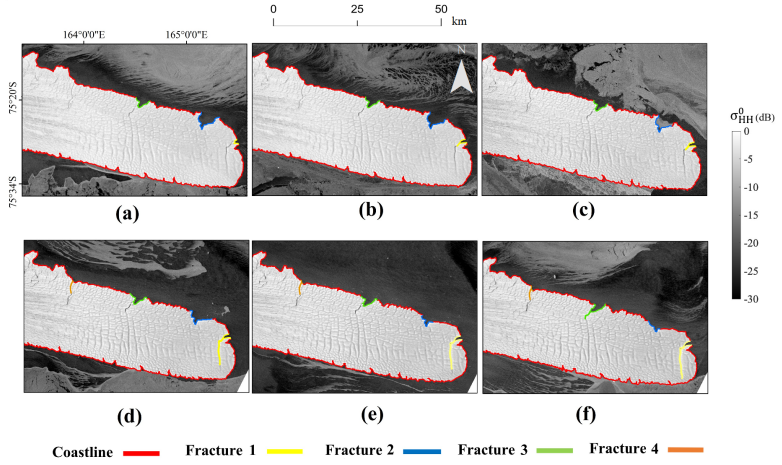

Figure 3.6 Coastlines extracted from the MDS that includes 6 scenes from 2016 to 2021 (panels (a) to (f), respectively). Each panel includes the extracted coastline overlaid, as a red line, onto the original HH-polarised SAR scene. Four ROIs are also highlighted and marked as "Fracture 1" to "Fracture 4" using different colors.

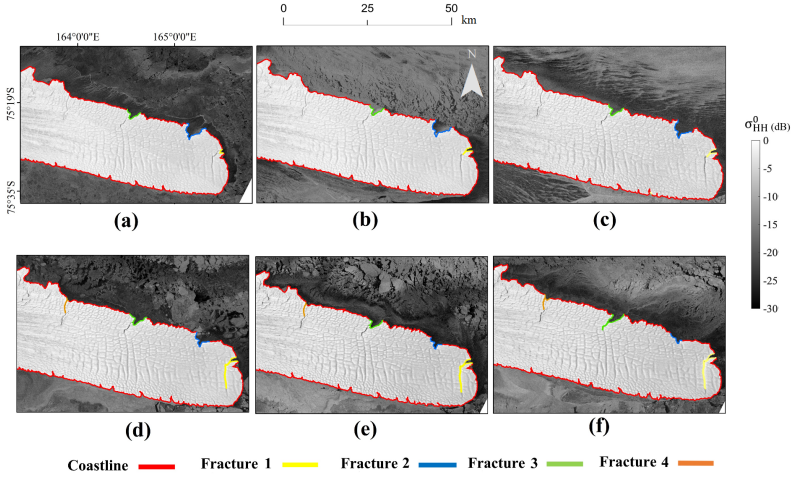

Figure 3.7 Coastlines extracted from the ADS that includes 6 scenes from 2016 to 2021 (panels (a) to (f), respectively). Each panel includes the extracted coastline overlaid, as a red line, onto the original HH-polarised SAR scene. Four ROIs are also highlighted and marked as "Fracture 1" to "Fracture 4" using different colors.

and the ice front moved toward the sea. This trend was already observed in the past [44, 49, 50], where it was pointed out that this atypical growing trend for an ice tongue finds its origin from the particular morphology of the Drygalski glacier area. In fact, the snow that fell over time has melted building-up until its weight resulted in snow compression, therefore turning it into ice. Hence, under the action of the accumulated ice, the glacier slowly flows down from the top towards the sea.

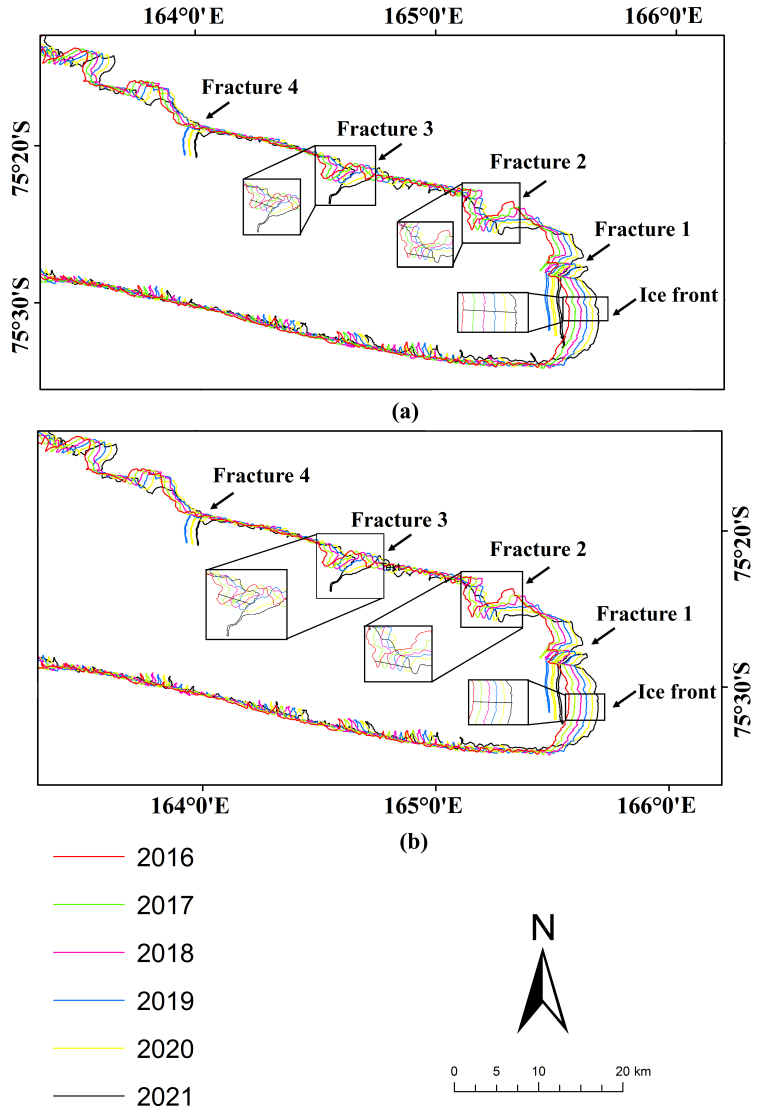

Figure 3.8 Extracted DIT profile depicted using different colors for: (a) MDS and (b) ADS. The features selected to estimate the displacement and the surface velocity are highlighted using black insets where the flow line used to select peer points is also annotated in black.

By comparing Figure 3.8 (a) and Figure 3.6, the following comments apply. Fracture "1" becomes larger and larger from 2016 up to 2021. The north-south rift that appears in the southern part of this fracture is detected by the extraction method starting from the scene collected in 2019. This implies that in 2019 the rift became large enough to be detected by the proposed method. Since 2019, the rift becomes larger and larger reaching the maximum in 2021, i. e., in the last SAR scene available in the data set. Figure 3.8 also shows that fracture "1" moves seaward for increasing time. This result agrees with the observations made in [51] using optical imagery. The fracture "2" appears to move seaward without any remarkable change in its shape up to 2018, while since 2018 it reduces its depth while still moving towards the sea. Fracture "3" does not

change its shape while moving seaward, with the only exception of the scene collected on 2021 that shows a deeper fracture (see the green ROI in Figure 3.6 (f) and the dark line in Figure 3.8). This elongated shape results from a rift which, although appears in all the SAR data set, becomes detectable by the proposed extraction method in 2021 only. Fracture "4" becomes visible in the extracted DIT profile from 2019 onward, moving towards the sea for increasing time. Similar comments apply for the ADS, see Figure 3.8 (b), that does not show remarkable differences with respect to the MDS. This further confirms the outcome of the short-term analysis showing that there is no significant change in the DIT morphology on a monthly basis. The main outcome stemming from the joint analysis of Figures 3.6 - 3.8 is that all the selected features move seaward for increasing time and some of them also change their shape.

The fourth experiment quantifies the DIT time variability by estimating the displacement and the average surface velocity of selected features over the entire long-term SAR data set. For a given feature, the displacement is evaluated by measuring the distance between a reference point and its corresponding peer identified on the extracted profile along the flow line after one year. The displacement is estimated considering as reference features the ice front and fractures "2" and "3", since their geometry remains sufficiently stable over time. Unlike fractures "1" and "4", which undergo significant morphological evolution (appearance, widening, or branching), fractures "2" and "3" preserve a consistent spatial configuration throughout the observation period. This geometric stability enables a reliable and reproducible identification of corresponding peer points along the flow line for displacement estimation. The displacements estimated from MDS and ADS are depicted in Figure 3.9(a) and (b), respectively, where red squares, blue asterisks, and green dots refer to the ice front, fracture "2", and fracture "3", respectively. In the MDS, the displacements range between approximately 530 m (fracture "3" in the period 2019–2020) and 720 m (fracture "2" in the period 2017–2018). Most features exhibit a displacement larger than 650 m for most yearly intervals over the reference period. The only exception is the period 2020–2021, during which the displacements lie in the range 550–650 m. The displacements estimated from ADS show a similar behaviour. In this case, the values span approximately from 525 m (fracture "2" in the period 2020–2021) to 800 m (fracture "2" in the period 2017–2018). Except for the period 2020–2021 and fracture "3" in the period 2018–2020, all features exhibit displacements larger than 650 m. The average surface velocities estimated from both MDS and ADS for the three selected features are listed in Table 3.3. In the MDS, the average surface velocity ranges from 614 m/year to 675 m/year, while in the ADS it

spans from 619 m/year to 667 m/year. Among the three features, fracture "3" exhibits the slowest motion, whereas the ice front shows the highest average surface velocity.

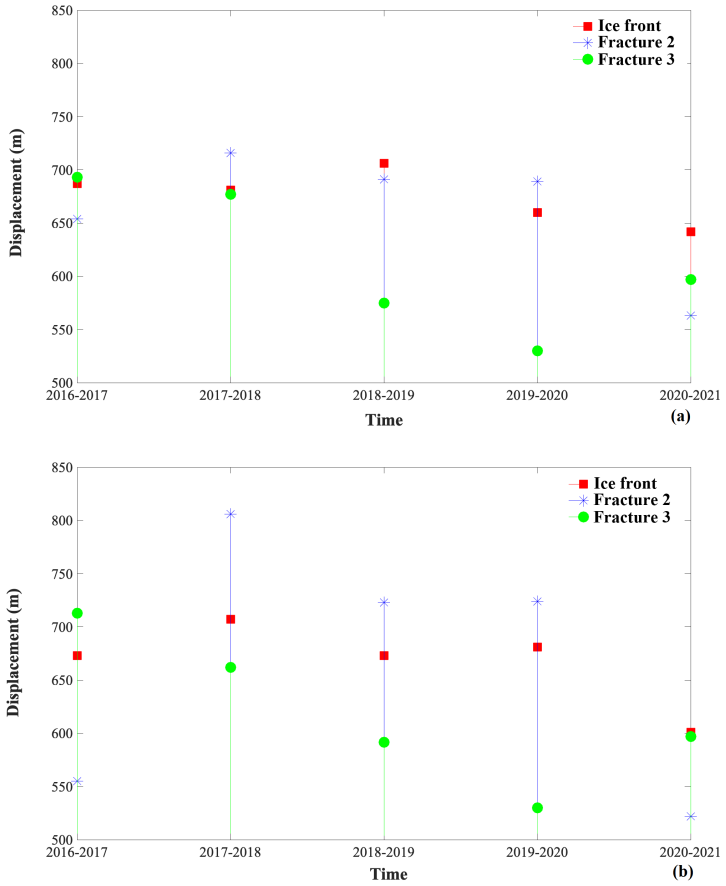

Figure 3.9 Displacement (in m) estimated from: (a) MDS and (b) ADS for the selected features.

By discussing the outcomes of this study with respect to the literature results listed in Table 3.3 one can note that:

- The DIT ice front moved with an average surface velocity of about 670 m/year during the period 2016–2021. This result agrees with the findings of [44, 50], who, using C-band SAR imagery, estimated average ice-front velocities ranging between 600 m/year and 733 m/year for the periods 1973–2012 and 1997–2000, respectively.
- A joint analysis of the results from this study and those reported in [44, 50] indicates that the DIT ice front has moved at a nearly constant rate over the past five decades.

Table 3.3 Summary of state-of-the-art satellite remote sensing studies on the DIT.

Author	Sensor	Time period	Feature	Average velocity (m/year)
M. Frezzotti and M. C. G. Mabin (1994)	Optical (Landsat 1 MSS, 4 TM)	1909–1993	Ice front	≈ 800 (1960–1993)
J. Wuite, K. C. Jezek *et al.* (2009)	SAR (Radarsat-1)	1997–2000	Ice front	≈ 733
NASA (2012)	Optical (Landsat 7)	1988–2002	Ice front	≈ 714
C. Zhao, X. Cheng *et al.* (2014)	SAR (Envisat ASAR) and Optical (Landsat ETM+)	1973–2012	Ice front velocity	≈ 600
C. Indrigo (2019)	Optical (Landsat 4, 5 TM, 7 ETM+, 8 OLI/TIRS)	1988–2018	Fracture/rift	647–689
		(2016–2018)		674–692
C. Indrigo, C. F. Dow *et al.* (2021)	Optical (Landsat 4, 5 TM, 7 ETM+, 8 OLI/TIRS)	1988–2020	Fracture/rift	≈ −550 – +685

- The SAR-based estimates presented here also agree with optical results derived from Landsat 7 imagery [49], where the ice front was found to advance seaward at an average rate of about 714 m/year between 1988 and 2012.
- Other DIT features show a time evolution that depends on the specific fracture considered. This agrees with the findings of [51]. As a general trend, the fractures moved seaward with an average velocity of about 640 m/year, which is consistent with the range of 647–689 m/year reported by [51] using optical data collected between 1998 and 2018.
- Restricting the analysis to the period 2016–2018 and focusing on fractures 2 and 3 (corresponding to fractures 1 and 2 in [52]), the average velocity obtained in this study, approximately 683 m/year, shows excellent agreement with the 692m/year and 674 m/year reported for those same features by [52].

3.2.5 Conclusive Remarks

In this study, we analysed the dynamics of the DIT (Antarctica) using Sentinel-1 C-band SAR images acquired from 2016 to 2021.The main findings can be summarised as follows:

- **Profile extraction:** The outline of the DIT was derived from Sentinel-1 HH-polarised C-band SAR data using an unsupervised CFAR approach, adapted to cope with both ice-free and ice-infested sea clutter.
- **Feature tracking:** The ice front and four main fractures along the northern margin were tracked throughout the observation record, enabling both short- and long-term assessments.

- **Short-term dynamics:** Month-to-month variations were minimal, indicating stable behaviour over short timescales.
- **Long-term evolution:** Between 2016 and 2021, the ice front advanced seaward at an average velocity of roughly 670 m/year, consistent with earlier independent estimates.
- **Fracture displacement:** The monitored fractures showed velocities between 615 and 680 m/year, confirming a coherent seaward progression.
- **Structural changes:** Since 2019, new rifts have appeared along the northern margin, suggesting emerging localised weakening within the ice tongue.
- **Link to ocean processes:** The dense Sentinel-1 time series provides the means to relate glacier and iceberg motion to broader ocean circulation, creating opportunities for integrated glaciological–oceanographic analysis.

Significance and alignment with aims. The findings from this chapter tie directly to the first two aims of the dissertation. In particular, the ability to extract the DIT outline under both ice-free and ice-infested conditions shows that C-band SAR can be used as a reliable tool for boundary delineation in Antarctica's difficult coastal setting. This directly addresses the first aim by confirming the ability of SAR features to distinguish between ice and the surrounding ocean and sea ice. In DIT, the tracking of the ice front and northern fractures across monthly and multi-year timescales provides new insights into both short-term stability and long-term dynamics, thereby fulfilling the second aim. Altogether, these findings demonstrate that Sentinel-1 C-band SAR is a dependable tool for the continuous monitoring of glacier and iceberg dynamics. Beyond meeting the objectives of this chapter, the results establish a firm foundation for the polarimetric analyses that follow. These findings do not mark an endpoint but rather a step forward in understanding how Sentinel-1 observations can be used to study Antarctic ice. They open the way for a closer examination of the physical structure and scattering behaviour of glaciers and icebergs. In this sense, the discussion naturally leads into the next stage of the dissertation, where the focus moves from boundary extraction and temporal tracking toward the application of polarimetric information to interpret scattering processes in greater detail.

Outlook. This section has mainly considered the gradual evolution of the DIT, but iceberg formation does not always follow such a slow process. In some cases, it can

occur suddenly as a result of strong geophysical events. The Hunga iceberg, formed after the volcanic tsunami in January 2022, is one such example that will be examined in future.

3.3 C33 iceberg monitoring

3.3.1 Study area

The large calving event occurred on 7 April 2016 that led to the formation of two large icebergs on the Nansen Ice Shelf (163°E, 75°S, Terra Nova Bay, Ross Sea, Antarctica) is investigated. The Nansen Ice Shelf flows into the Terra Nova Bay from the grounding line at the flow branch of the Reeves and Priestley glaciers for about 45 km to the front and is approximately 35 km across between the southern boundary, which is the northern side of the DIT and Inexpressible Island [53]. The collapse gave rise to two large icebergs: the largest one, termed as C33 by the National Ice Center, was about 21 km × 8 km, while the smallest one, namely C33b, was approximately 10 km × 5 km, see Figure 3.10. The calving area was estimated to be about 203 km^2 with an average thickness of 200 m and a mass loss of approximately 37 Gt (Giga tonne) [54]. After the calving, C33 and C33b icebergs drifted in the Terra Nova Bay with mélange attached, which once filled the large crevasse, along the Antarctic shoreline driven by ocean currents and winds.

3.3.2 SAR datasets

The SAR dataset includes four Sentinel-1 SAR imagery acquired from April to May 2016 in the IW dual-pol HH-HV mode. The geocoded SAR scenes that refer to the HH and HV channels are depicted in greytones using the decibel (dB) units in Figure 3.11 which is arranged into a matrix format. The two columns stand for co- and cross-polarization imagery. The four rows stand for the acquisition dates: 9 April 2016, 14 April 2016, 21 April 2016 and 3 May 2016, respectively, see Table 3.4. The area under investigation includes Terra Nova Bay and the C33 iceberg, which can be well-observed in the whole time series since it calls for a backscatter larger than the surrounding ice-covered area in both co- and cross-polarised channels. The clutter appears very inhomogeneous in both the channels with the co-polarised one resulting in the largest dynamic range. The cross-polarized backscatter resulting from the ice-covered area is very often below the Sentinel-1 system noise (i. e., about -22 dB). The imagery of Figure 3.11 show that the C33 iceberg drifted significantly in the

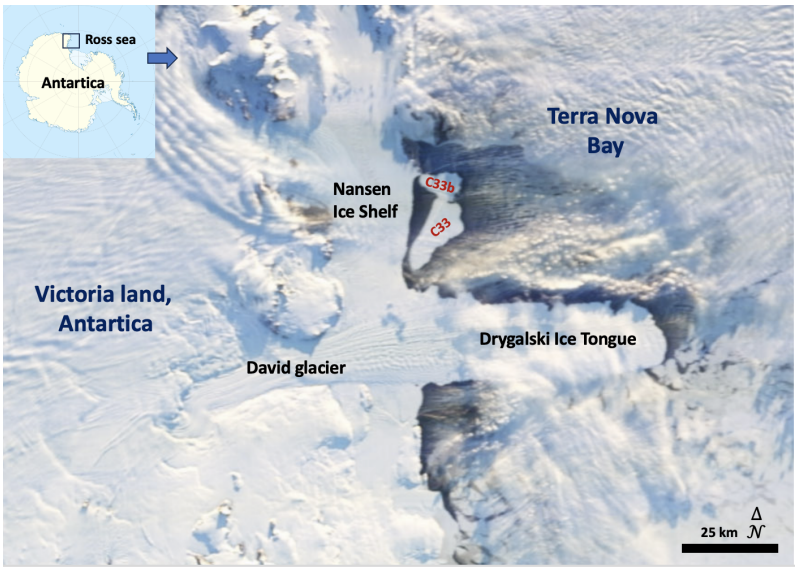

Figure 3.10 Optical image, partially obscured by clouds, taken on 7 April 2016 over the bay of Terra Nova by the sensor of the Moderate Resolution Imaging Spectroradiometer (MODIS) on board the Terra satellite. C33 and C33b icebergs, which have broken off from the Nansen Ice Shelf, can be recognized [3].

Terra Nova Bay during the observed time period. On 9 April 2016, i. e., two days after the calving, the iceberg is located just within the polynya which, as witnessed by the ice streaks aligned with the wind direction, is in its opening phase [20]. The iceberg then moved in the northern part of the Terra Nova Bay out of the polynya. By comparing co- (first column) and cross- (second column) polarized NRCS imagery one can note that the continental ice and the iceberg are very well visible in both the channels; while the ice-covered sea area calls for a co-polarized backscattering larger than the cross-polarized one, which is expected to result in the largest iceberg-to-clutter contrast.

Table 3.4 Summary of the Sentinel-1 SAR dataset used for the C33 iceberg analysis.

Acquisition date	Time (UTC)	Polarisation	Orbit pass	Incidence angle at C33 (°)
9 Apr 2016	11:02	HH+HV	Ascending	42
14 Apr 2016	11:10	HH+HV	Ascending	43
21 Apr 2016	11:02	HH+HV	Ascending	42
3 May 2016	11:02	HH+HV	Ascending	44

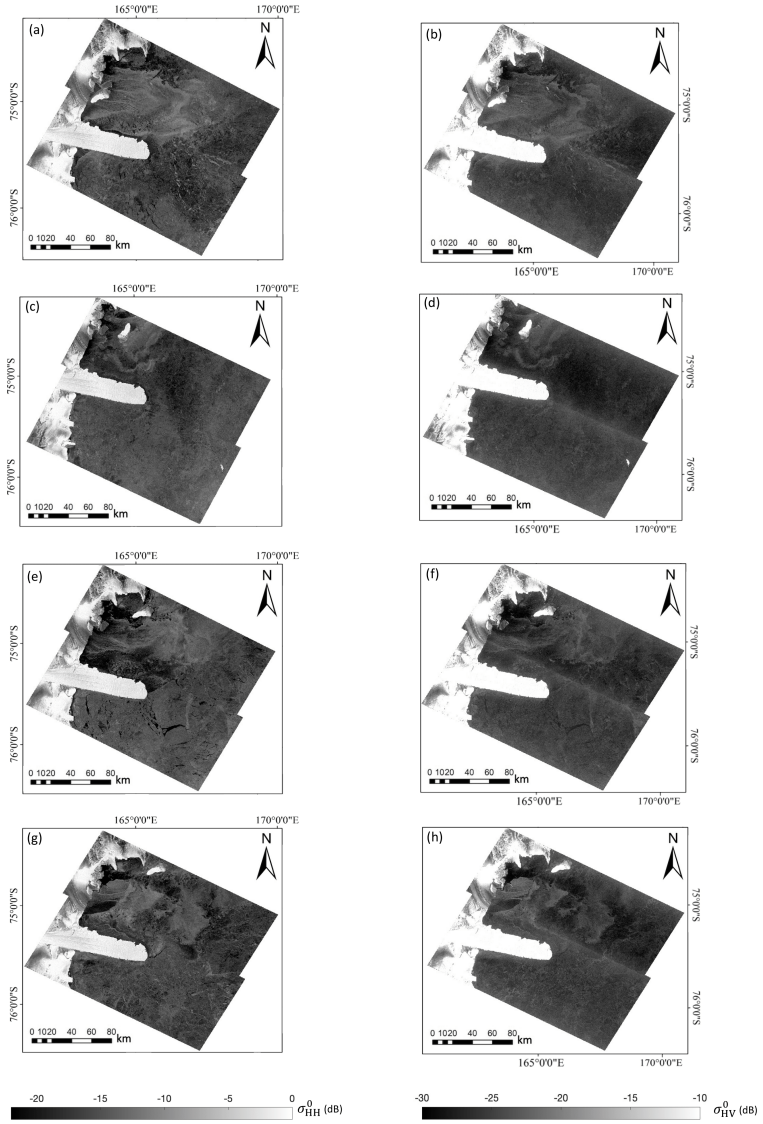

Figure 3.11 Sentinel-1 SAR dataset. The images are geocoded and shown in graytones using (dB) units. The image is arranged into a matrix format where rows correspond to the four acquisition dates—9 April, 14 April, 21 April and 3 May 2016 (top to bottom)—and columns correspond to the co- and cross-polarized backscattering channels.

3.3.3 Experimental results

Extraction of the C33 iceberg's profile

The iceberg's profile is extracted using σ^0_{HH}, σ^0_{HV} and r_{HV} (2.3). First, the sensitivity of the metrics with respect to the iceberg is analyzed focusing on the iceberg-to-clutter separability using, two ROIs excerpted over the iceberg and the surrounding clutter and measuring the distance $0 \leq d_m = \frac{m_{\mathrm{i}} - m_{\mathrm{c}}}{m_{\mathrm{i}}} \leq 1$, where m stands for the mean value of the adopted metric, i. e., σ^0_{HH}, σ^0_{HV} and r_{HV}, while the subscripts "i" and "c"

stand for an almost equal-size ROI excerpted over the iceberg and the surrounding clutter, respectively. The values of d_m are listed in Table 3.5 for the whole data set, quantitatively showing that the scattering response of the iceberg is very different from the clutter for all these metrics. The best performance is provided by the cross-polarized channel that results in the largest separation in all the imagery. To provide a deeper discussion of the iceberg-to-clutter separability, the empirical PDF is estimated within the two ROIs extracted using the SAR scene collected on 9 April 2016, see Figure 3.12. This SAR scene is the most demanding in terms of iceberg-to-clutter separability since, at that time, the C33 iceberg lied back in the polynya that calls for a very inhomogeneous backscattering. Figure 3.12, which shows the iceberg (gray color) and the clutter (cyan color) PDFs, demonstrates that the largest iceberg-to-clutter separation is provided by σ^0_{HV}. In addition, all the metrics call for a very spiky behavior over the clutter which results in a dynamic range significantly narrower than the sea ice. This witnesses that, although the iceberg appears almost uniformly brighter than the surrounding ice-covered clutter, its backscatter calls for a broader dynamic range. It can be also noted that lower backscatter values resulting from the iceberg almost completely overlap with the clutter's ones. To further quantitatively analyze the iceberg/clutter separability, the Wasserstein statistical distance is evaluated [55, 56]. The Wasserstein distance (also known as the Earth Mover's Distance) quantifies the minimum cost required to transform one probability distribution into another. In this context, it provides a physically meaningful measure of separability between the iceberg and clutter PDFs, with larger values indicating greater statistical distinction. For the SAR scene acquired on 9 April 2016, the Wasserstein distances between the iceberg and clutter distributions Figure 3.12 are 0.58, 1.71, and 1.24 for σ^0_{HH}, σ^0_{HV} and r_{HV} (2.3), respectively. This indicates that the cross-polarized backscattering channel provides the largest separability between the C33 iceberg and the surrounding clutter. Similar results are obtained when processing the entire data set (not shown for brevity).

Table 3.5 Iceberg-to-clutter separability based on the d_m metric, evaluated across the full dataset using iceberg and clutter ROIs.

SAR feature	**9 Apr 2016**	**14 Apr 2016**	**21 Apr 2016**	**3 May 2016**
$d_{\sigma^0_{\mathrm{HH}}}$	0.93	0.92	0.91	0.96
$d_{\sigma^0_{\mathrm{HV}}}$	0.97	0.98	0.97	0.99
$d_{r_{\mathrm{HV}}}$	0.95	0.96	0.95	0.98

This quantitative analysis suggests σ^0_{HV} to extract the C33 iceberg's profile in an objective and partially unsupervised way. A CFAR processing scheme is designed to

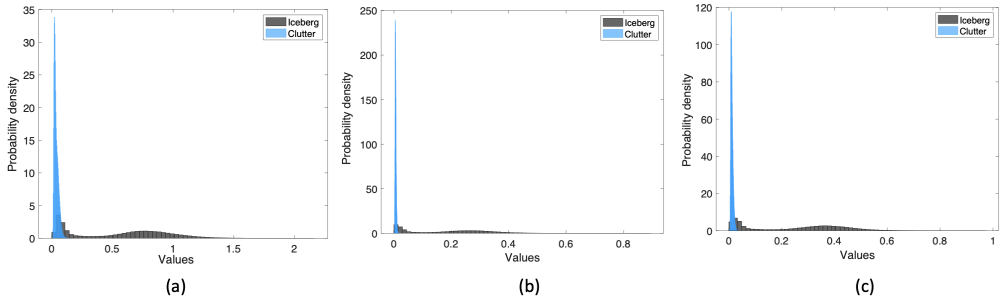

Figure 3.12 Empirical PDFs of (a) σ^0_{HH}, (b) σ^0_{HV}, and (c) r_{HV}, evaluated within the iceberg (gray) and clutter (cyan) ROIs. The x-axis represents the values of the corresponding polarimetric feature (in dB for HH and HV, and dimensionless values for r_{HV}), while the y-axis shows the probability density function (PDF).

binarize the Sentinel-1 imagery which is followed by morphological filtering to remove trivial false alarms resulting from the clutter or unwanted edges [53, 57]. The C33 iceberg is very big; hence, a global threshold CFAR approach is accurate enough to partition the image, with the global threshold set using a P_{fa} equal to 10^{-3} and modelling the clutter distribution using a Burr PDF. According to [58], the detection threshold related to the Burr clutter distribution is given by:

$$T = \left(\beta \left[P_{\mathrm{fa}}^{-\frac{1}{\alpha}} - 1\right]\right)^{\frac{1}{\mu}}, \tag{3.2}$$

where P_{fa} is the false alarm probability, α and μ are the non-negative shape parameters and β is the non-negative scale parameter. Once the binary image is obtained, trivial false alarms related to small clusters of pixels which are clearly not associated to the large C33 iceberg are removed by filtering out those isolated clusters consisting of less than $N = 1000$ pixels.

The binary map obtained processing the cross-polarized backscattering channel of the SAR scene collected on 9 April 2016 (see Figure 3.11 (b)) is shown in Figure 3.13 (a), where one can note that the continental ice and the iceberg are completely distinguished from the ice-covered sea area. The enlarged version of the area that includes the iceberg is depicted in Figure 3.13 (b); while the output of the morphological filtering is displayed in Figure 3.13 (c), where one can note that the iceberg is completely identified and the unwanted edges are removed. The C33 iceberg's boundary extracted using σ^0_{HV} related to the SAR scene collected on 9 April 2016, is superimposed as a red line over an enlarged version of the HH-polarized NRCS in Figure 3.13 (d). For

reference purposes, the iceberg's profile extracted using σ^0_{HH} and r_{HV} is also annotated using a cyan and yellow line, respectively.

By contrasting the profile extracted using the multi-polarization metrics with the profile visually inspected from the SAR image one can note that, as expected, σ^0_{HV} performs best since it results in a good trade-off between extraction accuracy and false alarms. The profile extracted using σ^0_{HH} results in performance similar to the σ^0_{HV} one, the main difference relies on the profile of the northern part of the iceberg (see the green star in panel (d)) that is not correctly extracted by the σ^0_{HH} and r_{HV} metrics. It must be explicitly noted that this part of the iceberg is very different from the rest of the iceberg in terms of backscatter intensity. This is probably due to the different geometrical and dielectric characteristics of that area. Similar extraction's performance is achieved when processing all the Sentinel-1 SAR scenes. The extracted C33 iceberg's profile agrees with the one obtained from the same data set using Markov Random Fields [59].

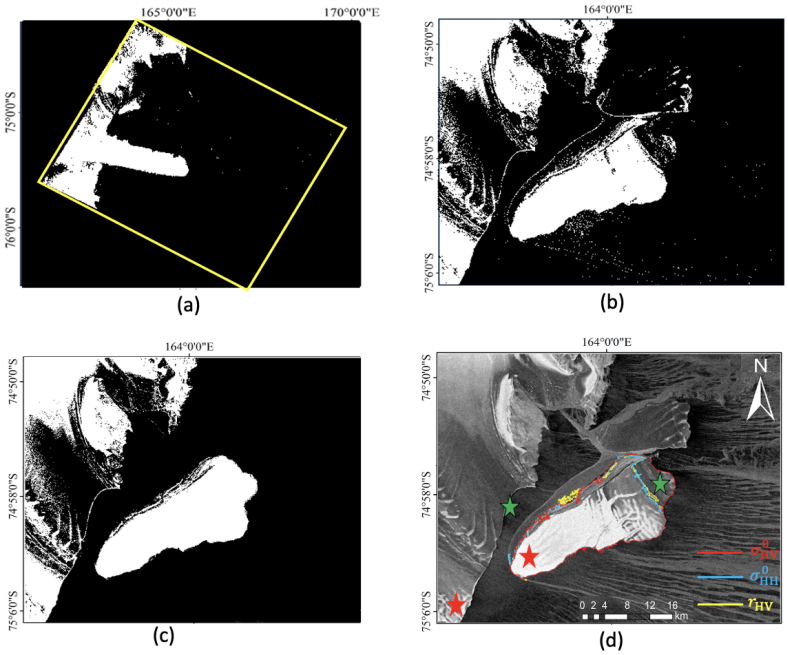

Figure 3.13 Processing of the SAR scene collected on 9 April 2016: (a) binary mask from σ^0_{HV}; (b) zoom on the C33 area; (c) mask refined with image-processing; (d) boundary from σ^0_{HV} (red), σ^0_{HH} (cyan), and r_{HV} (yellow), over the σ^0_{HH} graytones image. In (d), green/red stars mark the northern/southern parts of C33 on the Nansen Ice Shelf before calving and at the time of this SAR acquisition.

Tracking of the C33 iceberg

To track the C33 iceberg, the profile extracted applying the CFAR to the HV-polarized SAR data set is used. The iceberg positions along the whole time series are shown in a geocoded format in Figure 3.14 where, for each iceberg position, a reference point is selected to estimate the average surface velocity and the displacement. The reference point is automatically determined using the ArcGIS "Feature to Point" tool that allows creating a point feature representing the centroid of each polygon, i. e., the iceberg's center of gravity. In addition, from this point, a dashed yellow line is traced towards the narrower part of the iceberg to measure the heading of the iceberg with respect to the North.

Table 3.6 Dynamic parameters of the C33 iceberg estimated from the Sentinel-1 time series.

SAR image pair	**Displacement (km)**	**Velocity (km d^{-1})**	**Heading (°)**	**Area (km^2)**
9–14 Apr 2016	26.31	5.26	162	142.05
14–21 Apr 2016	25.54	3.64	203	137.78
21 Apr–3 May 2016	15.62	1.20	356	143.82
Whole period (9 Apr–3 May 2016)	67.47	2.81	–	143.75

The images of Figure 3.14 show that the C33 iceberg underwent a north-oriented trajectory during the observed time period drifting out of the Terra Nova Bay. The approximate length of the path followed by the iceberg is 67.47 km which was covered at about 2.81 km/day, see Table 3.6. In addition, the C33 iceberg underwent significant rotations during the drift in the Terra Nova Bay. The main axis (yellow arrow) is oriented along the: South-East direction on 9 April; North-East direction on 16 April and mostly along the South-North/South-West directions on 21 April and 3 May, respectively. These rotations are likely to affect the total displacement and the drift velocity. The area of the iceberg did not change significantly during the drift, see Table 3.6, where it can be noted that variations in the range of $\pm 4\%$ occurred which are likely to be within the area estimation error.

Polarimetric analysis of the C33 iceberg's properties

To provide a deeper understanding of the iceberg's properties, the DoP metric (2.5) is evaluated over the C33 iceberg area and depicted in Figure 3.15, which includes the scenes collected on: (a) April 9, (b) April 14, (c) April 21, (d) May 3, 2016.

As expected, the iceberg calls for very high depolarized backscatter that results in low DoP values. This implies that the iceberg calls for a weighted contribution of surface and volume scattering processes with the latter having a non-negligible weight

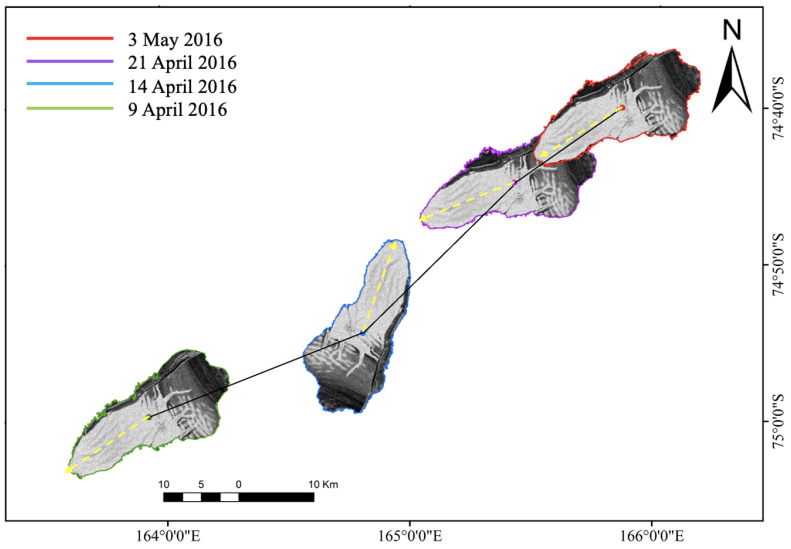

Figure 3.14 Estimated heading of the iceberg from the Sentinel-1 SAR dataset

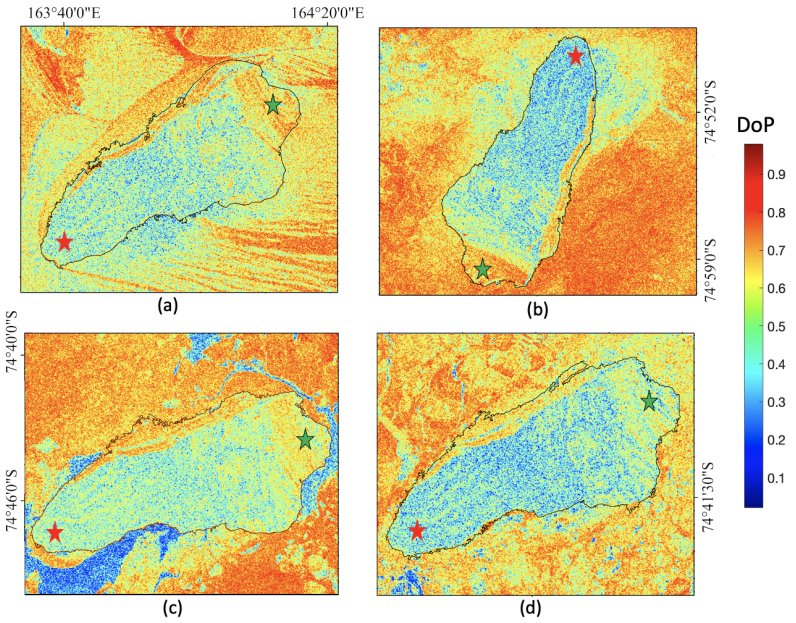

Figure 3.15 DoP within the C33 iceberg region of interest, evaluated using SAR scenes collected on: (a) 9 April, (b) 14 April, (c) 21 April, and (d) 3 May 2016. The iceberg's profile, extracted using σ^0_{HV}, is annotated as a black line for reference. In each panel, the green and red stars indicate the northern and southern parts of the C33 iceberg, respectively, as described in Figure 3.13(d).

in the total backscattered power. This applies in all the SAR scenes. By inspecting the whole data set, same peculiar behaviors can be identified. The C33 iceberg appears very inhomogeneous in terms of polarimetric scattering properties along the whole time series, showing a non negligible spatial and temporal variability. Hence, a quantitative analysis is performed locally by evaluating the mean DoP values over two different

iceberg regions: the northern (wider) and southern (narrower) part at the time of the first SAR acquisition, just after the calving event, see the green and red stars in Figure 3.13 (d), respectively. For convenience, they are annotated also in Figure 3.15.
The northern part of the C33 iceberg (see the green stars in Figure 3.15) results in a polarimetric scattering more polarized than the rest of the iceberg. On average, the DoP values estimated over this region are 0.71, 0.78, 0.65 and 0.61 on 9 April, 14 April, 21 April and 3 May 2016, respectively. Hence, the mean DoP value of that part of the iceberg is 0.69 during the drift. This means that, in this area, surface scattering mechanisms dominate the total backscattering which includes a significantly lower volumetric component. It is also worth noting that this area calls also for a co-polarized backscatter intensity almost overlapped with the one resulting from the ice-covered sea area as observed in the PDFs of Figure 3.12 (a) and in the time series of Figure 3.14. This implies that the iceberg's scattering properties in that area are very peculiar and almost indistinguishable, in terms of both intensity and polarimetric backscattering – from the surrounding ice-covered sea clutter. Note also that a non-negligible variability of the scattering properties is observed during the drift, since the average DoP values span from 0.61 to 0.78 over time.
Considering the southern part of the C33 iceberg (see the red stars in Figure 3.15 a completely different behavior in terms of polarimetric scattering properties is observed. In fact, the DoP values obtained in that area on 9 April, 14 April, 21 April and 3 May 2016 are, on average, 0.53, 0.48, 0.51 and 0.52, respectively. Hence, during the drift, the southern part of the iceberg is characterized by a mean DoP value of 0.51. This implies a more complicated scattering process where, together with a surface scattering component, a remarkable volumetric scattering mechanism contributes to the total backscattering. It can be also observed that the polarimetric scattering properties of that part of the iceberg are relatively stable over time, since the average DoP values span from 0.48 to 0.53 during the drift.
Actually, this difference between the northern and southern portions of the C33 iceberg was already visible before its calving from the Nansen Ice Shelf. In-situ photographs acquired from a helicopter in January 2012 (Figure 3.16) show that the northern sector was characterised by numerous small crests, channels, and melt ponds (panel b), whereas the southern sector appeared comparatively smoother at the macroscopic scale. However, it is important to emphasise that optical smoothness does not necessarily imply radar surface-dominated scattering. At C-band, the radar signal is sensitive to centimetre-scale roughness and internal structural heterogeneity, which can enhance depolarisation and volumetric contributions even when the surface appears visually

smooth. This explains the observed polarimetric behaviour and highlights the added value of dual-pol SAR measurements in capturing subsurface and structural variability beyond optical interpretation.

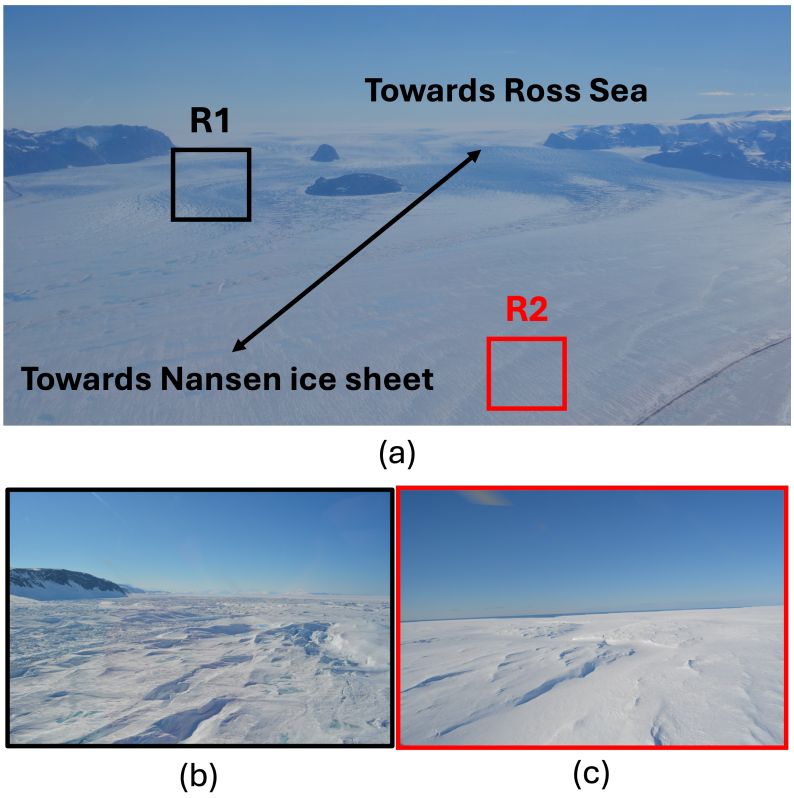

Figure 3.16 In-situ photographs of the Nansen Ice Shelf acquired from helicopter in January 2012, i.e., before the calving event. The areas enclosed in the black and red boxes, highlighted as R1 and R2 in (a), are enlarged in panels (b) and (c) and correspond to the northern and southern parts of the C33 iceberg, respectively.

3.3.4 Conclusive Remarks

This study focuses on the C33 iceberg originated by the calving event that occurred on 7 April 2016 on the Nansen Ice Shelf. The main findings can be summarised as follows:

- **Boundary extraction:** The cross-polarised HV channel provided the clearest separation between iceberg and surrounding ocean clutter, enabling robust delineation of the C33 outline.
- **Drift tracking:** Over the four acquisitions, the iceberg drifted along a 67 km path within Terra Nova Bay and experienced notable rotational movements, reflecting the influence of oceanic forcing.

- **Scattering mechanisms:** Polarimetric analysis revealed that C33's backscatter was best described by a weighted mix of surface (single- and oriented double-bounce) and volumetric scattering.
- **Spatial variability:** The scattering properties were not uniform across the iceberg surface but varied significantly, highlighting differences in structure and surface conditions.
- **Temporal evolution:** During the drift period, the scattering mechanisms changed in a non-uniform manner, indicating evolving interactions between the iceberg, atmosphere, and ocean environment.

Significance and alignment with aims. The C33 case study directly addresses both the first and third aims of this thesis. The accurate extraction of the iceberg boundary using polarimetric channels shows that C-band SAR has a remarkable ability to separate ice from the ocean, even in the most difficult Antarctic conditions, thus enabling the realization of the first objective. In parallel, the polarimetric analysis, particularly through parameters such as the DoP, offers new perspectives on the internal structure and dielectric heterogeneity of icebergs. Beyond these aims, the present study makes it clear that multipolarisation SAR data can reveal both the geometric dimension and the scattering properties of floating icebergs, a capability that contributes to a deeper understanding of their dynamics and underscores the scientific value of Sentinel-1 polarimetric observations.

Outlook. In this section, the results show that dual-pol, phase-based parameters such as the DoP can reveal useful information about how the iceberg scatters radar signals. However, to understand these patterns in more detail, further analysis is needed. Using additional polarimetric decompositions, such as the Cloude Pottier or Freeman Durden methods, would help separate the main scattering types surface, double-bounce, and volume. This approach would make it easier to see how different parts of the iceberg change over time and give a clearer sense of its overall structure and development.

Chapter 4

Canadian Environment

4.1 Introduction

This chapter presents the results of SAR analyses conducted in the Canadian Arctic and sub-Arctic, focusing on both glacier and inland lake environments. The main goal is to evaluate how dual-pol and CP SAR techniques perform in northern settings, where scattering behaviour is often complex and difficult to interpret. Building on the aims introduced in Chapter 1, three specific objectives are addressed.

First, the study examines the recent evolution of the d'Iberville Glacier on Ellesmere Island, Nunavut. A time series of Radarsat-2 and Sentinel-1 C-band SAR data is used to test how effectively multi-polarisation features can delineate the glacier front under sea-ice–infested conditions, while also quantifying changes in retreat rate, surface velocity, and overall area.

Second, attention shifts to inland lakes in the Canadian sub-Arctic. Using HP data from the RCM, the analysis focuses on Lake Athabasca and Bustard Island to explore how scattering behaviour differs between vegetated and sandy shorelines and under various imaging geometries. The aim is to assess whether hybrid-polarimetric features—both amplitude- and phase-based, offer measurable improvements in waterline detection compared with conventional single-pol data.

Finally, the chapter investigates polarimetric scattering behaviour across lake environments, focusing on parameters such as the wave degree of polarisation (m) and ellipticity. Particular attention is given to conditions where distinguishing land–water boundaries is most challenging, such as vegetated margins and sandy coasts, to evaluate how robust CP is for monitoring large northern regions.

This chapter includes two complementary case studies. The first, concerning the d'Iberville Glacier, is based on previously published work, while the second presents new

and unpublished analyses using RCM HP data. Similar to the Antarctic investigations in Chapter 3, each case study preserves the organisational structure of its original research. The glacier analysis features a dedicated methodology section, while the RCM investigation incorporates methodological details directly within the experimental discussion.

4.2 D'Iberville Glacier monitoring

4.2.1 Study area

The d'Iberville Glacier, one of the most important marine-terminating Arctic glacier, the d'Iberville glacier in the Canadian state of Nunavut (80.53 °N; 77.77 °W), see Figure 4.1(a). This study area represents a challening scenario with respect to the ones traditionally considered where to apply coastline/shoreline extraction method. The reason is twofold: from one side, the d'Iberville glacier is a marine-terminated glacier characterized by a particular coastal morphologyorography, i. e., it significantly differs from conventional "open area" as coastal harbours, ice tongues, rocky/sandy coasts; on the other side, the sea surface conditions significantly vary during the Arctic winter and summer and winter seasons (see the Sentinel-2 true color optical images in Figure 4.1 (b) and (c), respectively), for which the sea surface is completely frozen for most of the year due to the low temperature [60].

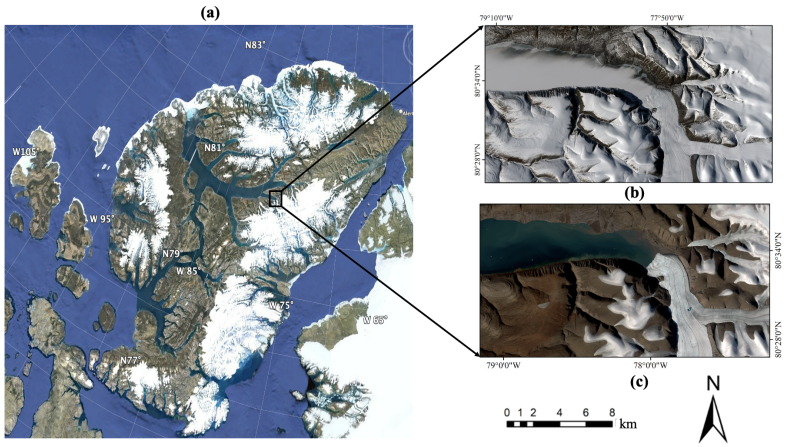

Figure 4.1 Study area. (a) Google Earth image of the study area that include the Ellesmere Island in the Canadian state of Nunavut. The black box refers to the ice front area of the d'Iberville glacier, considered for quantitative analysis. Sentinel-2 true color optical images collected over the ice front of the d'Iberville glacier on: (b) 26 May 2021 and (c) 26 July 2020.

4.2.2 Remote sensing dataset

For the purposes of this study, C-band SAR data from two satellite missions, namely the Canadian Space Agency Radarsat-2 and the European Space Agency Sentinel-1, are considered. Three Radarsat-2 SAR scenes are collected over the study area in dual-po fine imaging mode (HH+HV, i. e., an horizontally-polarised electromagnetic wave is transmitted while the backscattered wave is measured on an orthogonal horizontal-vertical polarization linear basis) from 2010 to 2012 (one scene per year). Seven Sentinel-1 SAR scenes are collected over the study area in dual-pol HH+HV Interferometric Wide Swath (IW) imaging mode. from 2015 to 2022 (one scene per year but 2016). The main characteristics of SAR satellite data are listed in Table 4.1. Independent optical data from the European Space Agency Sentinel-2 mission, whose satellites are equipped with a Multispectral Imager (MSI), where also collected over the d'Iberville glacier. When they were sufficiently cloud-free and time collocated (within $\pm$ 3 days) with the SAR scenes, they are used to assess the accuracy performance of the ice front extraction methodology.

Table 4.1 Overview of the satellite SAR datasets used for monitoring the d'Iberville Glacier.

SAR mission	Number of scenes	Imaging mode	Polarisation	Pixel spacing (m)	Acquisition period
Radarsat-2	3	Fine	HH+HV	6	2010–2012
Sentinel-1	7	IW	HH+HV	13	2015–2022

4.2.3 Methodology

In this section, the methodology adopted to extract the ice front of the d'Iberville glacier and to analyse its dynamics is presented. The methodology has a twofold objective: 1) the extraction of the glacier's ice front, i. e., the boundary between the marine-terminated glacier and the frozen/unfrozen sea surface, from a single SAR image using both single- and dual-pol features; 2) the evaluation of the behavior of the ice front over time to estimate its advancing/retreating. A flowchart of the processing chain is shown in Figure 4.2, where three main steps can be identified.

- **Pre-processing step**. All the SAR scenes from the data set are preprocessed using the SNAP (Sentinel Application Platform) v 8.0 software: to reduce orbital errors, speckle noise and geometric distortions. First, radiometric calibration is performed and, then, a 5 $\times$ 5 sliding window si applied to reduce speckle, which may hamper the identification of the ice front. Finally, range doppler terrain correction is applied to map the SAR imagery in geographical coordinates,

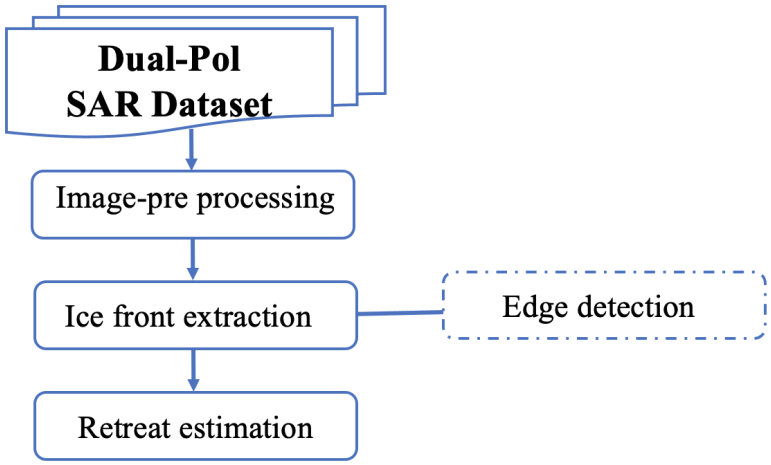

Figure 4.2 Flowchart of the proposed methodology.

resulting in a square pixel whose spacing is 6 m and 13 m for Radarsat-2 and Sentinel-1, respectively.

- **Ice front estimation step**. A CFAR approach is used to distinguish the d'Iberville glacier from the surrounding ice-free or ice-infested sea water, i. e., to extract the ice front. The CFAR is applied on the HH-polarised NRCS (Normalised Radar Cross Section), indicated with σ^0_{HH}, and on a combination of the HH- and HV-polarised scattering amplitudes, termed as r_{HV} (2.3). As a result, the CFAR algorithm automatically provides a global threshold for the σ^0_{HH} and r_{HV} images, thus generating a binary image. The latter is refined by conventional image processing tools, i. e., morphological filters, to sort out clear and isolated false edges at sea. Then, the optimal Canny edge detector, which is based on a two-dimensional Gaussian kernel, is applied on the refined binary image to obtain the actual ice front of the d'Iberville glacier. A more detailed description of the processing chain is reported in previous studies [31, 61], where similar approaches were applied to a variety of coastal and glaciated settings.

- **Retreat estimation step**. Once the first two steps were applied on the whole SAR data set, the ten ice fronts extracted for the d'Iberville glacier are imported in ArcGIS software to quantitative estimate the retreat.

4.2.4 Experimental results

This section presents the results obtained from three experiments. The first experiment consisted of analysing the sensitivity of the single- and dual-pol features (2.3) to the

different scattering scenarios, i.e., frozen and ice-free sea surfaces (see Figure 4.3 (a)(d) respectively). The second experiment aimed to investigate the accuracy performance of the ice front extraction of σ^0_{HH} and r_{HV} under both sea conditions in order to find the feature that achieved the lowest root mean square error (RMSE) between the extracted ice front and the reference one manually extracted from the corresponding Sentinel-2 optical images. The third experiment consisted of analysing the temporal behaviour of the d'Iberville Glacier ice front using quantitative indicators such as the ice front surface velocity and the amount of ice surface gain/loss.

For the purpose of the first two experiments, two SAR scenes collected under different sea-surface conditions were selected from the data set according to the shortest time gap between the SAR and MSI acquisitions (see Figure 4.3). The first one refers to the observation in May 2021 during the winter season when the sea surface was completely frozen due to very low temperatures (see the Sentinel-2 true-colour optical image in Figure 4.3(a)). The corresponding σ^0_{HH} and r_{HV} images are depicted as graytones and false-colour images at the decibel (dB) scale in Figures 4.3b,c, respectively. The second scene is relevant to the acquisition in July 2020 during the summer season when the sea surface was completely ice-free due to relatively higher temperatures (see the Sentinel-2 true-colour optical image in Figure4.3(d)). The corresponding σ^0_{HH} and r_{HV} images are shown in Figures 4.3(e)(f), respectively.

The first experiment consisted of the analysis of the sensitivity of σ^0_{HH} and r_{HV} to ice-free and ice-infested sea surfaces. By visually inspecting Figure 4.3, it can be seen that the separability between the marine-terminating d'Iberville Glacier and the frozen sea surface is challenging, even in the Sentinel-2 optical image, making the extraction of the ice front not straightforward. When dealing with the HH-polarised NRCS images, it can be observed that both the frozen and unfrozen sea surfaces appear as almost homogeneous areas that are darker than the terminus of the glacier, which, instead, shows some roughness in the surface pattern. In addition, the difference in backscattering between the sea surface and the glacier appears larger in the unfrozen case than in the case when the sea surface is ice-infested. In fact, in the latter case, the two regions look very similar, except for on the ice front, which appears as a brighter edge. When dealing with the r images, similar comments apply.

To perform a quantitative multi-polarisation backscattering analysis, two equal-sized ROIs consisting of 100×100 pixels were randomly selected from the sea and glacier areas close to the ice front (see the cyan and white squares, respectively, which are annotated in Figures 4.3 (a),(d)). The statistical behaviours estimated for σ^0_{HH} and r_{HV} for the selected ROIs under both frozen and unfrozen sea conditions are shown

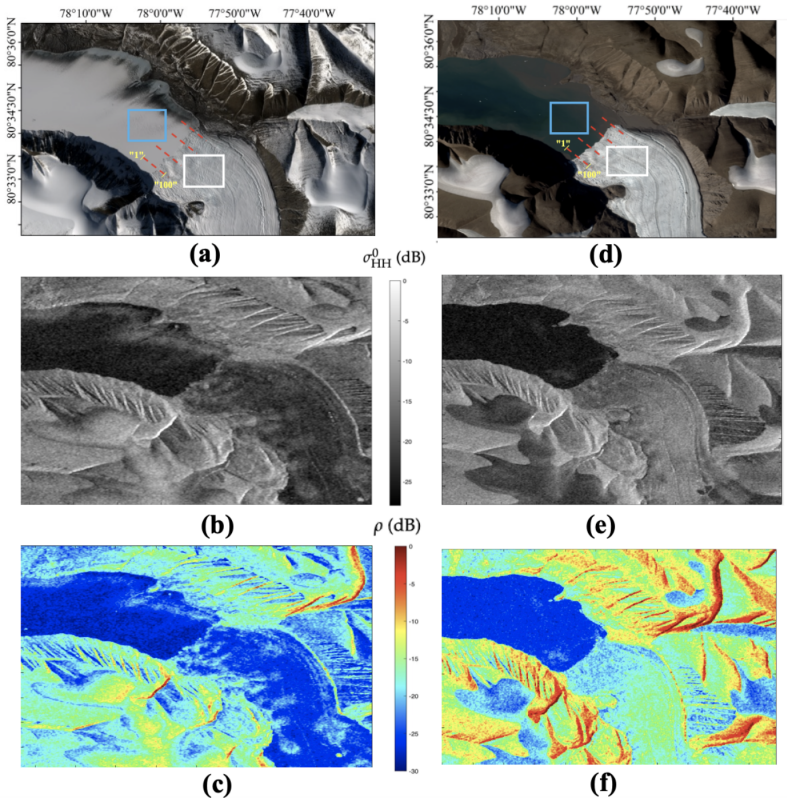

Figure 4.3 Showcased scenes for frozen (left) and ice-free (right) sea-surface conditions. Rows from top to bottom: Sentinel-2 true colour optical image; σ^0_{HH} in dB scale; r_{HV} in dB scale. Cyan and white boxes in (a) and (d) indicate the sea and glacier ROIs used for quantitative analysis.

in Figure 4.4, where experimental histograms are depicted using blue (sea ROI) and orange (glacier ROI). In Figure 4.4, the rows refer to the unfrozen and frozen cases, whereas the columns refer to σ^0_{HH} and r_{HV}. The corresponding mean and standard deviation values of σ^0_{HH} and r_{HV} are listed in Table 4.2. The mean contrast is also annotated as a rough indicator of the separability between the sea and glacier ROIs in terms of multi-polarisation backscattering.

Table 4.2 Mean and standard deviation values of σ^0_{HH} and r_{HV} in frozen and unfrozen cases, evaluated over the ROIs in Figure 4.3. Contrast refers to the difference between sea (Area 1) and glacier (Area 2).

SAR feature	Case	Area 1 (Sea)	Area 2 (Glacier)	Contrast (dB)
σ^0_{HH}	Unfrozen	-24.1 ± 1.0	-15.4 ± 1.1	8.7
r_{HV}	Unfrozen	-26.4 ± 0.7	-21.2 ± 0.9	5.2
σ^0_{HH}	Frozen	-22.4 ± 1.0	-18.5 ± 1.3	3.9
r_{HV}	Frozen	-25.1 ± 0.8	-22.0 ± 1.1	3.1

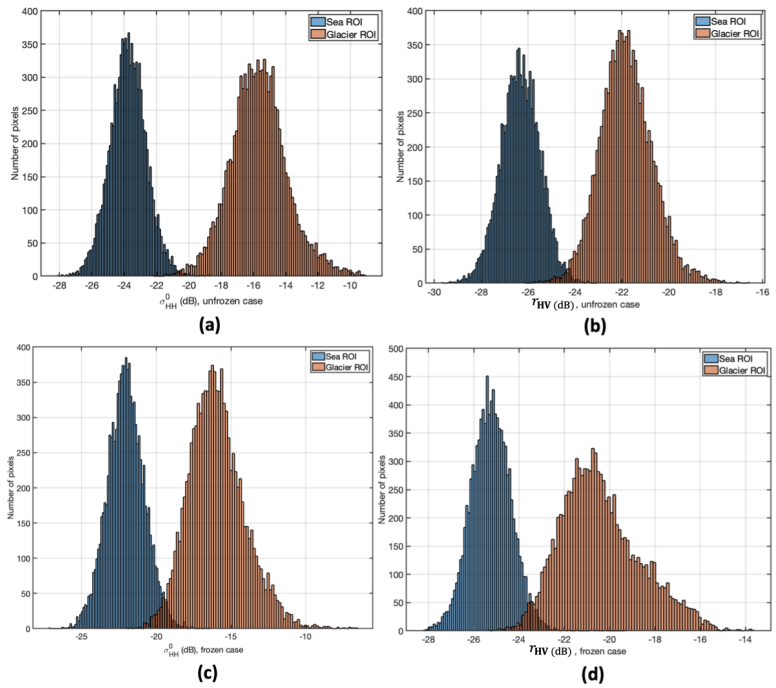

Figure 4.4 Statistical behaviour of single- and dual-pol features evaluated for the 104 samples belonging to the selected ice-free and ice-infested sea (blue) and glacier (orange) ROIs. Rows correspond to histograms for the unfrozen (a,b) and frozen (c,d) cases, while columns refer to σ^0_{HH} (a,c) and r_{HV} (b,d). The corresponding mean and standard deviation values are reported in Table 4.2.

When dealing with the unfrozen case, for the seawater ROI, σ^0_{HH} and r_{HV} had average values of about -24 dB and -26.5 dB, whereas they increased to approximately -15.5 dB and -22 dB, respectively, for the glacier ROI. This resulted in a mean contrast, which was no lower than 4.5 dB on average for both features. Nonetheless, it is worth noting that the mean contrast between the seawater and glacier ROIs provided by σ^0_{HH}, i.e., 8.1 dB, was more than 3.5 dB higher than the one evaluated from r_{HV} (4.5 dB).

When dealing with the frozen case, σ^0_{HH} and r_{HV} were characterised by average sea (glacier) ROI values of about -22 dB and -25 dB (-16 dB and -20.5 dB). This resulted in a mean contrast of 6.1 dB and 4.8 dB for σ^0_{HH} and r_{HV}, respectively, proving that even in this case, the HH-polarised NRCS provided a higher glacier/ice-infested seawater separability.

A deeper analysis was undertaken by evaluating the behaviour of σ^0_{HH} and r_{HV} along four randomly selected transects crossing the sea/glacier boundary. They are annotated as red dashed lines in Figure 4.3a,d. The transects consisted of 100 pixels each, where pixels "1" and "100" refer to the transect's sea and glacier pixels farthest from the ice front, respectively (see yellow labels in Figure 4.3a,d), whereas the latter

was at pixel number "50". The results relevant to the ice-free and ice-covered sea surfaces are shown in Figure 4.5, Figure4.6, respectively, where black and blue dashed lines refer to the σ^0_{HH} and r_{HV} values obtained after averaging along the four transects. In addition, for reference purposes, the mean values evaluated for the sea and glacier ROIs are shown in Figure 4.3a,d and Table 4.2, and they are annotated using the same colour coding but with continuous lines.

When dealing with the unfrozen case, it can be observed that the σ^0_{HH} values were in the range of about -25 to -22 dB for the ice-free sea surface, whereas for the glacier, they increased to approximately -18 to -12 dB (see Figure 4.5). Considering the dual-pol feature r_{HV}, values from about -27 to -26 dB were observed for the unfrozen sea, whereas they increased to a range of approximately -23 to -19 dB for the glacier.

Considering the frozen case, different comments apply (see Figure 4.6). In fact, even though the glacier area was closer to the ice front (pixel number "50"), the σ^0_{HH} and r_{HV} values were almost the same as those observed for the unfrozen case; the freezing of the sea surface resulted in a different multi-polarisation backscattering that yielded slightly higher values (about +2 dB) for both the single- and dual-pol features.

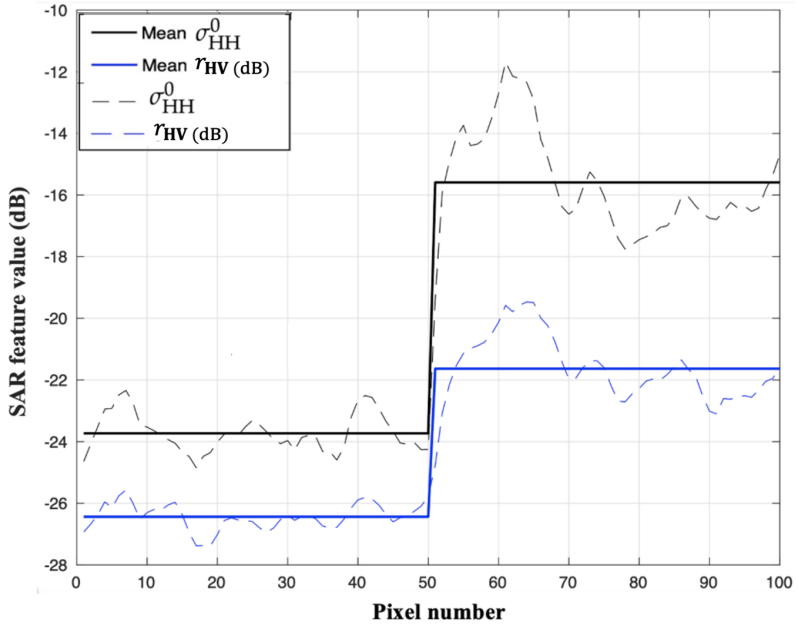

Figure 4.5 Unfrozen case. Dashed lines show σ^0_{HH} (black) and r_{HV} (blue) values averaged over the four transects indicated by red dashed lines in Figure 4.3a,d. For reference, the mean values of σ^0_{HH} (black) and r_{HV} (blue) estimated for the sea and glacier ROIs (see Table 4.2 and Figure 4.3a,d) are plotted as continuous lines.

The second experiment consisted of evaluating the accuracy of the methodology used for extracting the d'Iberville Glacier ice front. The performance of the σ^0_{HH}

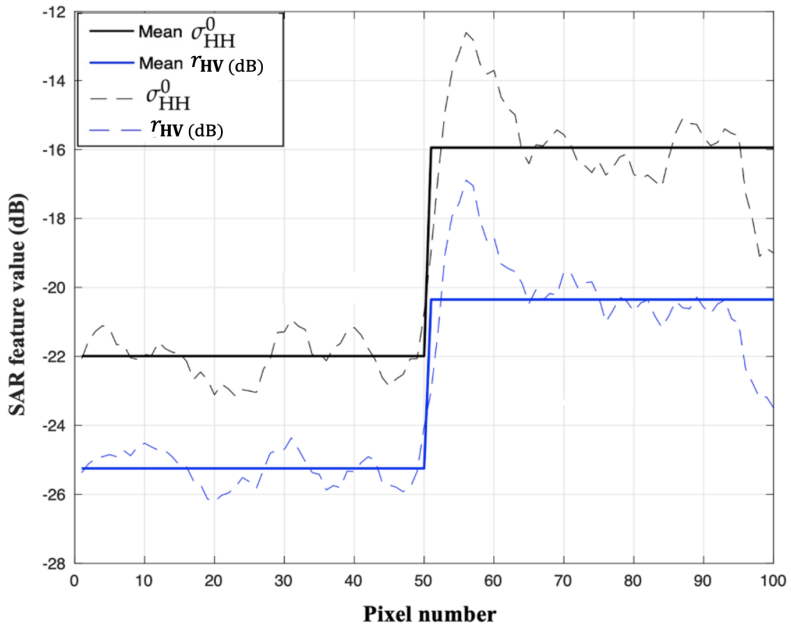

Figure 4.6 Frozen case. Dashed lines show σ^0_{HH} (black) and r_{HV} (blue) values averaged over the four transects indicated by red dashed lines in Figure 4.3a,d. For reference, the mean values of σ^0_{HH} (black) and r_{HV} (blue) estimated for the sea and glacier ROIs (see Table 4.2 and Figure 4.3a,d) are plotted as continuous lines.

and r_{HV} features was analysed under both frozen and unfrozen sea conditions. The quantitative assessment was based on the root mean square error (RMSE) values estimated between the ice front extracted from the SAR imagery and the ice front manually traced from the corresponding reference Sentinel-2 true-colour optical images.

The results relevant to the unfrozen case are shown in Figure 4.7, where the ice fronts extracted from σ^0_{HH} and r_{HV} (depicted in red and green, respectively) are overlapped on the reference optical image. An inset is also shown to better highlight the results (see the yellow box). It can be seen that the ice fronts extracted from both features resulted in good visual agreement with the actual ice front profile obtained from the optical image, even though some non-negligible false alarms occurred along the north-eastern edge of the d'Iberville Glacier ice front. A visual inspection also suggests that σ^0_{HH} achieved slightly higher accuracy compared to r_{HV}, consistent with the findings of the first experiment.

To perform a quantitative analysis, 20 points were randomly selected along the ice fronts, and the RMSE was evaluated between the corresponding points belonging to the ice fronts extracted from the SAR images (σ^0_{HH} and r_{HV}) and those manually traced from the Sentinel-2 optical reference. The results showed that σ^0_{HH} achieved an RMSE of 1.18 pixels, whereas r_{HV} had an RMSE of 2.97 pixels.

The same analysis was performed for the frozen case (see Figure 4.8). As expected, due to the more challenging scattering conditions, larger RMSE values were obtained, namely 3.35 pixels for σ^0_{HH} and 4.56 pixels for r_{HV}.

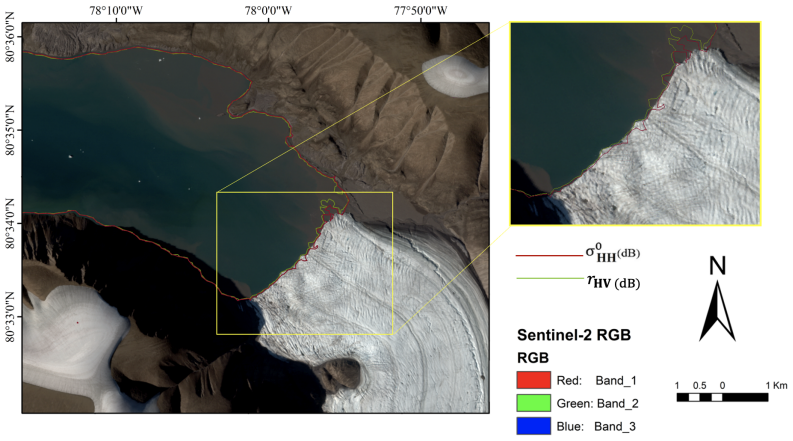

Figure 4.7 Accuracy assessment of the ice front extraction in the unfrozen case. Ice fronts extracted from σ^0_{HH} (red) and r_{HV} (green) are overlaid on the reference optical (RGB) image collected by the Sentinel-2 MSI on 26 July 2020. An enlarged version, highlighted by the yellow box, is included to better illustrate the results.

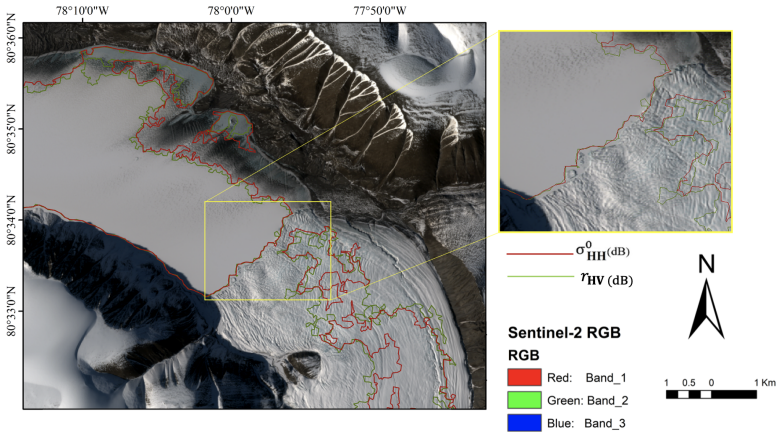

Figure 4.8 Accuracy assessment of the ice front extraction in the frozen case. Ice fronts extracted from σ^0_{HH} (red) and r_{HV} (green) are overlaid on the reference optical (RGB) image collected by the Sentinel-2 MSI on 26 May 2021. An enlarged version, highlighted by the yellow box, is included to better illustrate the results.

The third experiment consisted of investigating the temporal behaviour of the d'Iberville glacier ice front from 2010 to 2022. On the basis of the results of the previous experiments, the ice front was extracted from the HH-polarised NRCS images of the whole SAR data set. The results are shown in Figure 4.9, where the study area is masked in white, except for the 10 ice fronts extracted from σ^0_{HH}, which are

depicted using different colours. Figure 4.9 clearly shows that the d'Iberville glacier exhibited a net retreat over the last 12 years (see the red and yellow ice fronts that refer to 2010 and 2022, respectively). To quantitatively analyse the retreating rate of the d'Iberville glacier, the average surface velocity was estimated by measuring, for each couple of consecutive years in the SAR data set, the distance between the two ice fronts computed from the same points randomly selected for the evaluation of the RMSE divided by the number of years. The average surface velocity estimated in such a way is listed in Table 4.3. It can be seen that the retreating rate of the d'Iberville glacier varied significantly over time. In fact, the very fast retreat during 2010–2011, when the d'Iberville glacier had an average surface velocity of 514 m/year, corresponds to the almost stable behaviour of the d'Iberville glacier during 2021–2022, when it was characterised by an average surface velocity of 28 m/year. However, on average, from 2010 to 2022 the d'Iberville glacier retreated with an average surface velocity of 160 m/year. Together with the average surface velocity, the net ice loss from the glacier's surface was estimated by measuring the area between the ice fronts extracted in 2010 and 2022 (see Figure 4.10), where the extent of the retreat is highlighted in cyan. The latter corresponds to an ice area of about 2.2 km^2, meaning that, on average, the d'Iberville glacier experienced an ice loss of about 0.18 km^2 per year from 2010 to 2022.

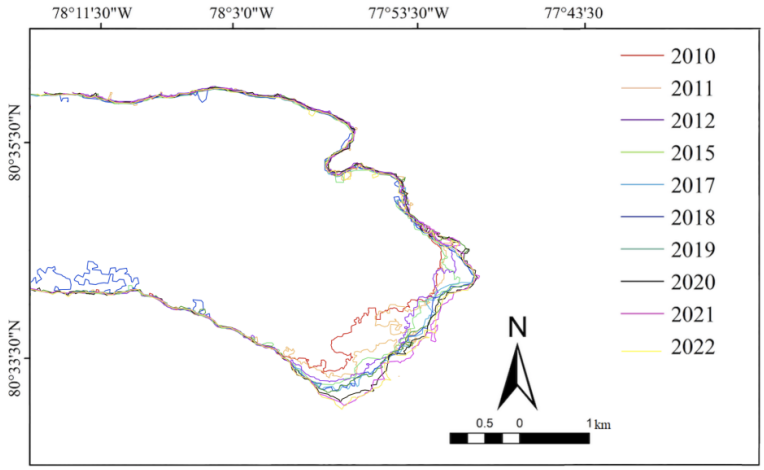

Figure 4.9 Ice fronts of the d'Iberville glacier extracted from σ^0_{HH} from 2010 to 2022

Previous research on the d'Iberville Glacier consistently points to its ongoing retreat, but the actual rate has changed a lot over the years. For example, [62] used aerial photos from 1975 to estimate a retreat of about 480 meters per year, a pace much faster than what we've seen in more recent times. C-band SAR measurements from 1991 gave a lower but still substantial value of about 300 m/year [63]. More recent analyses, conducted between 1999 and 2004, suggested a slowdown, with retreat rates

Table 4.3 Average retreating surface velocities of the d'Iberville Glacier ice front estimated from the experimental results shown in Figure 3.9.

Year	Surface Velocity (m per year)
2010–2011	514
2011–2012	326
2012–2015	81
2015–2017	90
2017–2018	108
2018–2019	136
2019–2020	196
2020–2021	142
2021–2022	28

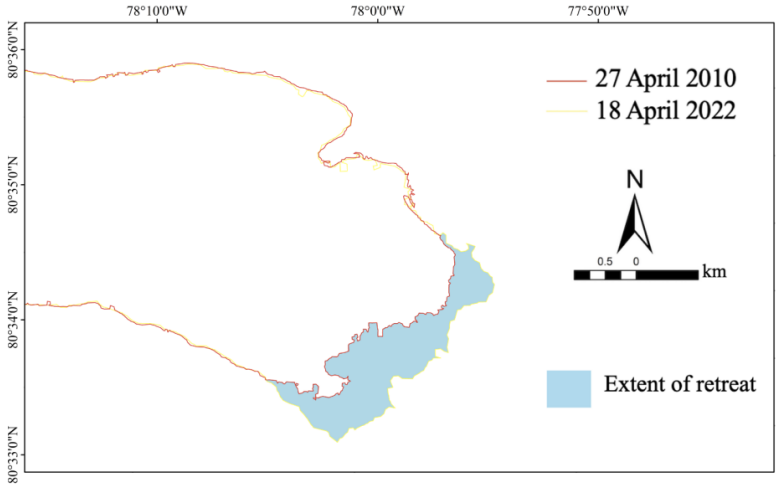

Figure 4.10 Estimation of the d'Iberville glacier retreat extent obtained from the ice fronts extracted in 2010 and 2022 from σ^0_{HH}.

ranging from 30 to 105 m/year [64, 65]. These values are much closer to the rates we derived for the period 2010–2022. A longer study spanning 1999–2015 also confirmed the glacier's continuing retreat, although the results were expressed in terms of ice mass discharge rather than frontal velocity [66].

When compared with neighbouring glaciers, the behaviour of d'Iberville fits within the regional pattern but stands out in terms of magnitude. On Ellesmere Island, about three-quarters of the marine-terminating glaciers retreated between 1999 and 2015, with an average frontal velocity of roughly 150 m/year [66], which is consistent with the mean of 160 m/year that we report. What really sets d'Iberville apart is how much ice it's losing. Our estimate, 0.18 km^2 per year, is about 50% higher than the regional average of 0.12 km^2 per year across 252 glaciers in the North Canadian Arctic

[67]. Even if we just look at the years 2010–2020, d'Iberville's retreat is still around 54% faster than the regional trend. So, while this glacier is following the same general pattern as its neighbours, it's shrinking at a noticeably faster rate, which suggests it's especially sensitive to changes in its environment.

4.2.5 Conclusive Remarks

The dynamics of the d'Iberville Glacier (Ellesmere Island, Nunavut) were investigated using Radarsat-2 and Sentinel-1 C-band SAR images acquired between 2010 and 2022. The main findings can be summarised as follows:

- **Profile extraction.** The proposed method successfully delineated the glacier front under both frozen and open-water conditions. In practice, the HH-polarised NRCS (σ^0_{HH}) provided a clearer distinction between the glacier terminus and the surrounding sea surface than the dual-pol parameter r_{HV}. Errors were generally within five pixels of the optical reference, confirming the reliability of the SAR-based extraction.

- **Accuracy performance.** Both single- and dual-pol features enabled the glacier front to be traced, but σ^0_{HH} consistently achieved higher separability, particularly in winter when frozen sea surfaces reduced contrast. Although accuracy declined slightly under these more complex conditions, the position of the ice front could still be identified with reasonable confidence.

- **Temporal variability.** Between 2010 and 2022, the glacier retreated at an average rate of approximately 160 m/year. Retreat was most pronounced in 2010–2011 (≈514 m/year), while the 2021–2022 interval showed near-stability (≈ 28 m/year). Overall, the glacier lost an estimated 2.2 km^2 of ice, equivalent to roughly 0.18 km^2, per year.

Significance and alignment with aims. These findings relate directly to the second aim of this dissertation, showing that dual-pol SAR can be used to monitor glacier changes under Arctic conditions, where sea ice is often present. Comparing σ^0_{HH} with r_{HV} also links to the third aim, since it reveals how polarimetric parameters respond differently depending on the sea-surface state. Overall, the d'Iberville study demonstrates a practical way to monitor glacier fronts and sets the groundwork for applying CP to lake environments and for testing polarimetric features in other northern monitoring settings.

Outlook. The analysis of the d'Iberville glacier confirms the value of SAR for long-term retreat monitoring, but the next step is to scale up. Applying the same framework to a wider set of marine-terminating glaciers across the Canadian Arctic would enable a more systematic view of regional ice loss. In addition, the use of oceanography and climatology information opens the door to a richer understanding of what drives glacier retreat. Therefore, we can understand how the story unfolding at d'Iberville fits into the much bigger picture of Arctic change.

4.3 Sub-Arctic Lakes monitoring

4.3.1 Study areas

In this section, a set of experiments relevant to lakes waterline is described. The lakes that are examined in this study are environmentally different to best describe the diversity of such waterlines. In particular, four sub-areas in Alberta, Canada, as shown in Figure 4.11, are analyzed. Four study areas are considered: two vegetated coastal sites, one in the southwestern part of Lake Athabasca (Case 1) and another in Lake Ryan (Case 2); and two sandy coastal sites, one on Bustard Island in Lake Athabasca, within the Fidler-Greywillow Wildland Provincial Park (Case 3), and the other in the southeastern region of Lake Athabasca (Case 4). Before proceeding further, we provide a brief description of Lake Athabasca, Ryan Lake, and Bustard Island.

Lake Athabasca

Lake Athabasca lies on the border between Alberta and Saskatchewan in Canada, directly south of the Northwest Territories [68]. The lake spans approximately 335 km in length and 51 km in width, covering an area of about 7,936 km^2, with a maximum depth of 124 metres [68]. It is fed from the southwest by the Peace and Athabasca Rivers, whose delta separates Lake Athabasca from Lakes Claire and Mamawi. The lake drains northwest via the Slave River, which flows into the Arctic Ocean through Great Slave Lake and the Mackenzie River. The southwestern part of Lake Athabasca is characterized by dense vegetation and sandy beaches, making it an ideal site for studying waterline dynamics and ecosystem interactions.

Bustard Island

Bustard Island, located within the Fidler-Greywillow Wildland Provincial Park in Lake Athabasca, serves as a critical habitat for various bird species and features extensive

Figure 4.11 Geographical location and case study areas around Lake Athabasca, Ryan Lake, and Bustard Island: vegetation and sandy coasts.

sandy beaches [69]. These beaches, which are prone to seasonal flooding and erosion, provide an excellent case study for analyzing coastal dynamics.

Ryan Lake

Ryan Lake is situated in the Northern Boreal (Nb4) zone of Alberta, at approximately 59°11'N, 111°5'32"W, covering an area of 603.9 hectares (6 km^2). Located near the southern shore of Lake Athabasca, the lake is characterized by vegetated shores [70].

4.3.2 SAR datasets

The RCM is an advanced Canadian satellite system consisting of three identical C-band SAR sensors. It is designed for frequent Earth observation with a revisit time of four

days. The system supports multiple spatial resolutions ranging from highly detailed 1-metre resolution imagery in Spotlight to a lower resolution of 100 m with ScanSAR mode.

The RCM offers twelve imaging modes, each with distinct characteristics such as spatial resolution, swath width, and noise floor. All modes support single, dual, and compact (hybrid) polarisation options. Additionally, RCM includes a dedicated full polarimetric imaging mode. These different imaging capabilities make RCM extremely versatile for applications such as marine monitoring, sea ice mapping, disaster response and land use classification. The HP mode is of special relevance in this study; it transmits a right-circularly polarized wave, receiving two linear orthogonal ones, i.e., H and V.

In this study, we processed a set of eight SLC RCM HP images acquired using the StripMap beam mode with a nominal spatial resolution of 16 m. These data were acquired during an ascending orbit pass and using RCH and RCV polarizations in right-looking mode. For the four case studies, we selected images with Low Angles of Incidence (Low AOI) and High Angles of Incidence (High AOI), as summarized in Table 4.4. To further analyze the cases in question, the SAR RCM HP dataset is enriched by external measurements. Sentinel-2 RGB imagery and NDVI have been considered. The NDVI maps are used to assess vegetation distribution. The NDVI results confirmed the presence of dense vegetation in specific areas, where higher NDVI values distinguished vegetated regions from adjacent land and water surfaces. Similarly, Sentinel-2 RGB imagery highlighted the sandy beach areas with their distinct bright signatures, clearly separating them from vegetated and water regions. These combined validations ensured the reliability of the selected regions for further analysis, accurately representing both vegetation and sandy beach areas as shown in Figure 4.12. For each study site, Sentinel-2 datasets were acquired within a temporal window of one week before or after the corresponding SAR acquisitions.

The nominal noise equivalent sigma zero (NESZ) of the RCM CP StripMap modes ranges between -17 dB for the very high resolution and -25 dB for the 16m spatial resolution mode. However, the actual noise was found to be at least 4 dB better than the nominal. This system noise ensures sufficient sensitivity for detecting targets with low backscatter, such as water surfaces and smooth terrain, while maintaining robustness for vegetation and coastal studies. The improved NESZ across all CP modes contributes to the reliability of RCM data for quantitative remote sensing applications, including classification and change detection. Several studies have validated the performance of

Figure 4.12 Comparative analysis of vegetated and sandy shorelines using Sentinel-2 RGB and NDVI data.

Table 4.4 Summary of RCM HP SAR data used for the sub-Arctic lake case studies.

Case study	Coast type	Satellite	Acquisition date	Incidence angle (°)
Lake Athabasca (1)	Vegetated	RCM 2	13 Jul 2023	38–40 (High AOI)
		RCM 3	16 May 2023	20–22 (Low AOI)
Ryan Lake (2)	Vegetated	RCM 2	1 Jul 2023	38–40 (High AOI)
		RCM 3	16 May 2023	20–22 (Low AOI)
Bustard Island (3)	Sandy	RCM 1	3 Jun 2023	40–42 (High AOI)
		RCM 3	9 Jun 2023	20–22 (Low AOI)
Lake Athabasca (4)	Sandy	RCM 1	3 Jun 2023	40–42 (High AOI)
		RCM 3	28 May 2023	22–24 (Low AOI)

the RCM CP modes and confirmed its stability and suitability for Earth observation applications [71] and [72].

4.3.3 Experimental results

This section presents the SAR-based analysis of lake waterlines using HP data acquired by the RCM. The analysis focuses on seasonal observations across various landscapes, including sandy coasts and vegetated shorelines, under different angles of incidence. The following subsections describe the dataset characteristics, preprocessing steps, and the polarimetric parameters used to assess waterline dynamics.

A.Vegetated Coasts

For each case study, the RH and RV graytones squared modulus, i.e. the Normalized Radar Cross Section (NRCS), of RCM HP SAR images are shown. A window size of 5 $\times$ 5 pixels was used to estimate both the RH and RV channels in (2.7). The same 5 $\times$ 5 averaging window was consistently applied during the computation of the Stokes parameters, ensuring uniform spatial smoothing across both polarimetric channels.

The format of Fig. 4.13, is consistent across all cases: the left column displays the high AOI cases, while the right column shows the low AOI cases. Panels (a) and (c) correspond to the RH images, and panels (b) and (d) correspond to the RV images.

In high AOI observations, as shown in Fig. 4.13 (a) and (b), there is a clear contrast between land and water. At higher incidence angles, the radar signal interacts more effectively with the vegetation canopy, penetrating deeper and enhancing volume scattering within the vegetation. This leads to stronger backscatter from vegetated areas. At the same time, the electromagnetic's interaction with water surfaces is dominated by specular reflection, which significantly suppresses backscatter from water. This combination of enhanced volume scattering in vegetation and reduced surface scattering from water creates a strong contrast, making the boundaries between vegetation and adjacent water bodies distinct and easy to be detected. In contrast, the low AOI observations shown in Fig. 4.13(c) and (d) exhibit limited contrast between land and water. At lower incidence angles, the radar signal interacts more with surface features, making the SAR sensor more sensitive to surface roughness. In vegetated areas, the surface roughness of vegetation and water surfaces can appear similar in the radar signal, reducing the difference in backscatter. As a result, boundaries between vegetation and adjacent water bodies are less pronounced in low AOI imagery, making land-to-water discrimination more challenging.

To further investigate the scattering behaviour shown in Fig. 4.13, we analyzed external information about the local wind over the lake. For both SAR images, acquired on 13 July 2023 at 01:04 (a–b) and on 16 May 2023 at 00:48 UTC time (c–d),

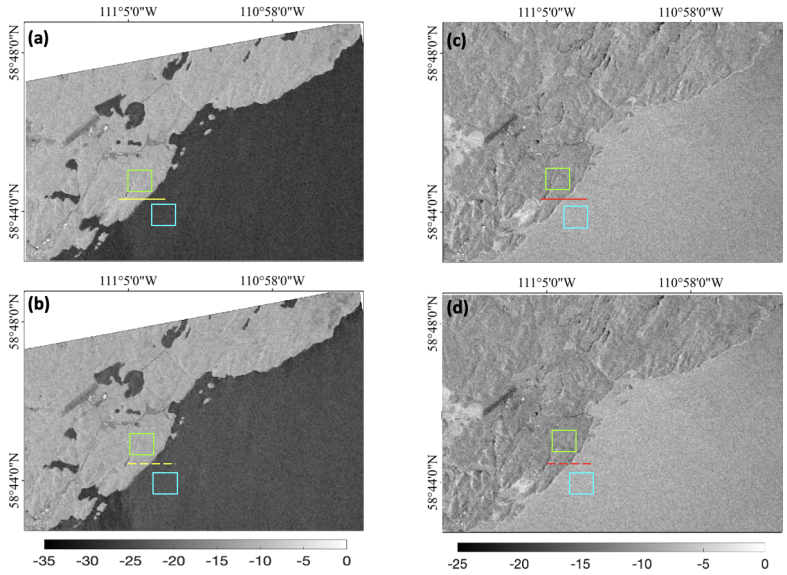

Figure 4.13 NRCS images for case study 1 at high and low AOI. Panels (a) and (b) correspond to the high AOI acquisition, while panels (c) and (d) correspond to the low AOI acquisition. The same transect used for profile extraction is overlaid on all images. For visual clarity, it is displayed as a dashed yellow line in panels (a) and (b) and as a dashed red line in panels (c) and (d). The green and cyan boxes denote the representative ice and water reference areas, respectively. All images are shown in grayscale using a decibel (dB) scale.

independent wind data were retrieved from the Fort Chipewyan RCS station, located approximately 10 km from the study area. On 13 July, the wind speed was about 19 km/h at 01:00 UTC time, with only a 4-minute difference from the SAR acquisition time. On 16 May, wind speeds ranged between 18–20 km/h from 00:00 to 01:00 UTC time, corresponding to a maximum time difference of 12 minutes. Although spatial and temporal colocation is not exact, analysis of external data supports the assumption that wind speeds are relatively low to moderate during both acquisitions and almost identical, so that the two acquisitions are basically not dependent on wind speed. In both cases, no rain was present and the wind direction was similar.

Building on the observations in Fig. 4.13, we conducted a more detailed quantitative analysis. First, a large area of 2,322 pixels encompassing both water and vegetation regions was quantitatively analyzed in terms of histograms (see Fig. 4.14). The overall histogram plots for RH and RV polarizations under both high- and low-AOI conditions are shown in Fig. 4.14. These histograms confirm the increased separability between water and vegetation at high AOI and the reduced contrast at low AOI, particularly in the RH polarization. Furthermore, a quantitative transect analysis was conducted using the same transect shown in Fig. 4.13, to illustrate differences in scattering behavior between high and low AOI observations. As shown in Fig. 4.15, the profiles agree with

the expected performance of backscattering under varying AOI conditions. Specifically, the contrast is more pronounced in high-AOI observations and becomes less distinct at low AOI. Over water, the backscatter difference between high and low AOIs reaches up to approximately 15 dB, while over vegetation it remains within 2 dB.

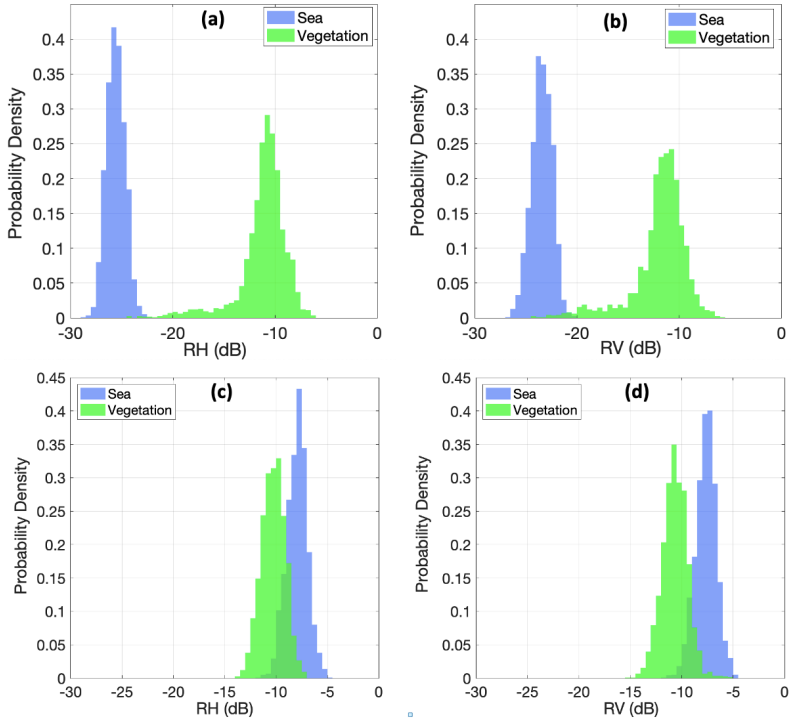

Figure 4.14 Histograms of vegetation (green) and water (blue) for case study 1, corresponding to the selected rectangles in Fig. 4.13. Panels (a) and (b) show the RH and RV RCM channels under high-AOI conditions, respectively, while panels (c) and (d) correspond to the same channels under low-AOI conditions.

Having established the backscattering characteristics through the NRCS analysis, we next investigate the polarimetric behavior to better exploit the information available from m (2.10), EP (2.11), EP-STD (2.12).

Building on the observations in Fig. 4.16, we extend the analysis beyond backscatter intensity to examine the polarimetric indicators derived from RCM HP data. Following the approach used in the NRCS analysis, a total of 2,322 pixels crossing the waterline, as shown in Fig. 4.13, were quantitatively evaluated in terms of histograms of the EP and its (EP_std), as presented in Fig. 4.17. Panels (a) and (b) correspond to high-AOI conditions, while panels (c) and (d) correspond to low AOI conditions. The blue bars represent water pixels, and the green bars represent vegetation pixels. The histograms confirm that under low AOI conditions, water pixels exhibit very stable polarimetric behavior, with EP values approaching unity and low variability

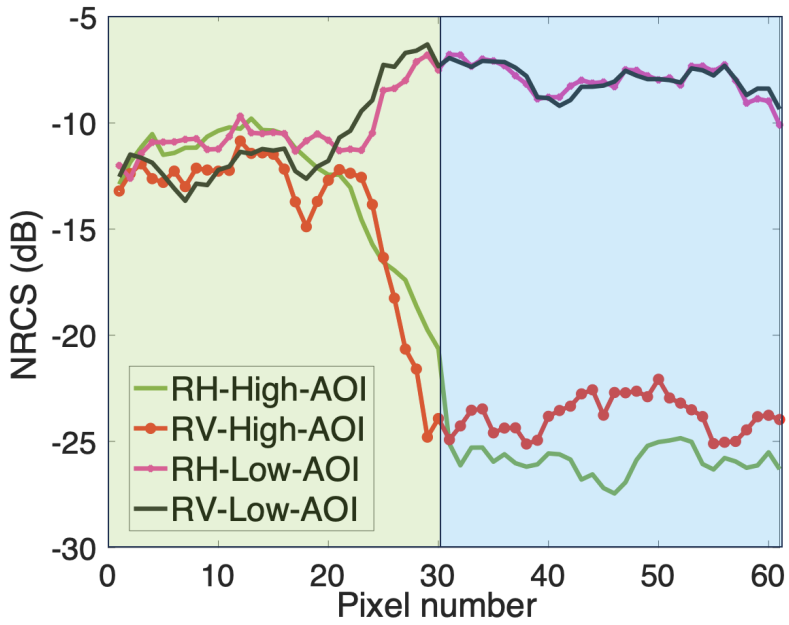

Figure 4.15 Plots of RH and RV NRCS (in dB) along the transect, see selected lines in Fig. 4.13. The green-shaded area indicates the vegetated region, while the blue-shaded area corresponds to the open water.

(EP_std near zero). Conversely, vegetation pixels show broader distributions and lower EP values, indicating greater scattering complexity. At high AOI, both EP and EP_std distributions broaden, reflecting higher polarimetric variability, particularly over vegetation surfaces. To complement the statistical analysis based on histograms, a spatial examination was also performed to better capture localized variations in polarimetric behavior across the waterline. This transition from area-based statistics to transect-based profiles enables a direct comparison of polarimetric stability and contrast along the land–water boundary. In this subsequent analysis (see Fig.4.18), corresponding to the Low AOI condition, features m and the EP are shown along a representative transect. Although the histograms in Fig.4.17 are based on EP and EP_std, the transect plots in Fig.4.18 use EP and m.

To quantify these qualitative observations, the mean EP and EP_std values were computed for each case study and surface type under both Low and High AOI conditions. These results, summarized in Table 4.5, provide a statistical evaluation of the polarimetric stability and enable direct comparison between water and vegetations surfaces. Each value was computed from the same 2,322-pixel sample used in the histogram analysis.

A second independent vegetated waterline was also investigated (Fig. 4.19), corresponding to case study 2 (see Table 4.4). The NRCS analysis presented in Fig. 4.19 is

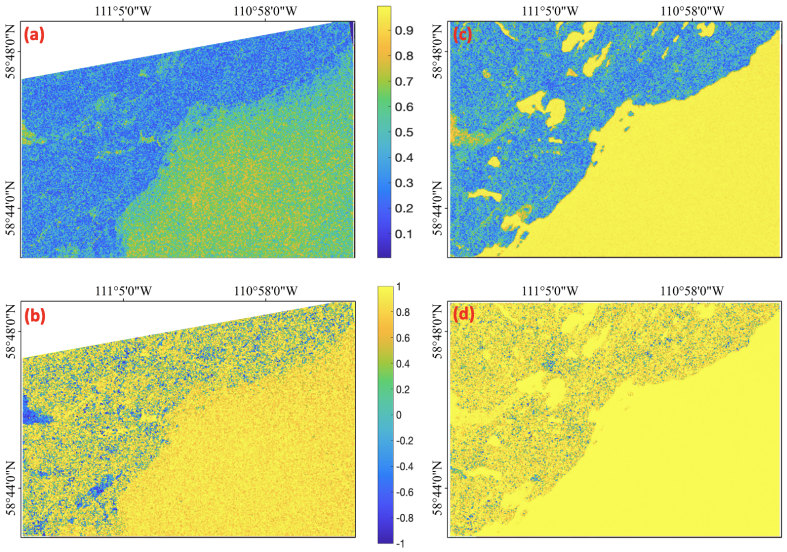

Figure 4.16 Polarimetric features maps relevant to case 1. On the left (right) column the High (Low) AOI are considered. In (a) and (c) m is shown, in (b) and (d) the EP.

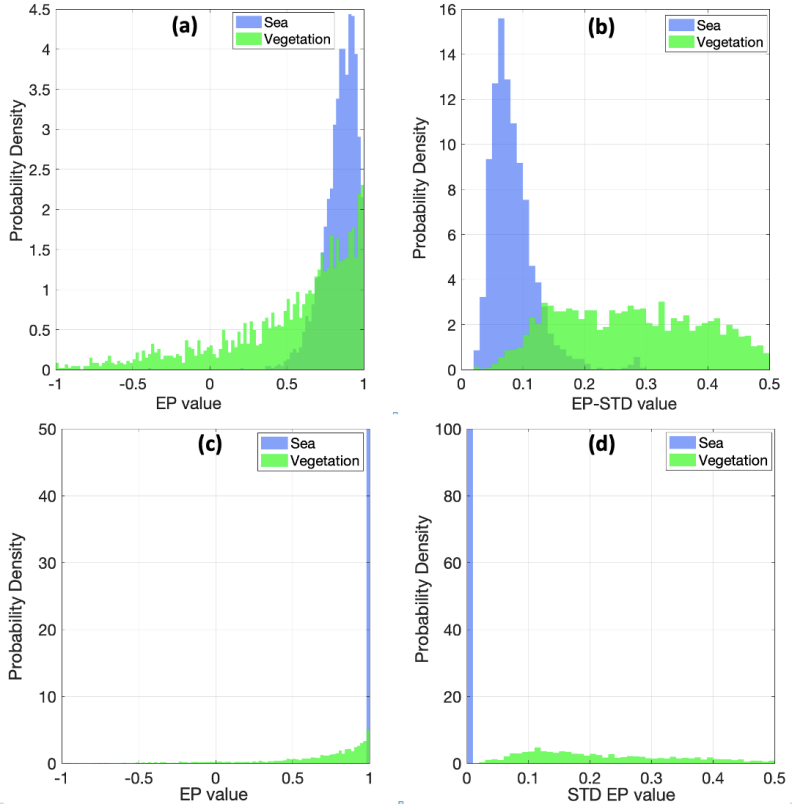

Figure 4.17 Histograms of vegetation (green) and water (blue) for case study 1, corresponding to the selected rectangles in Fig. 4.13. Panels (a) and (b) show the EP and EP_std under high-AOI conditions, respectively, while panels (c) and (d) correspond to the same channels under low-AOI conditions.

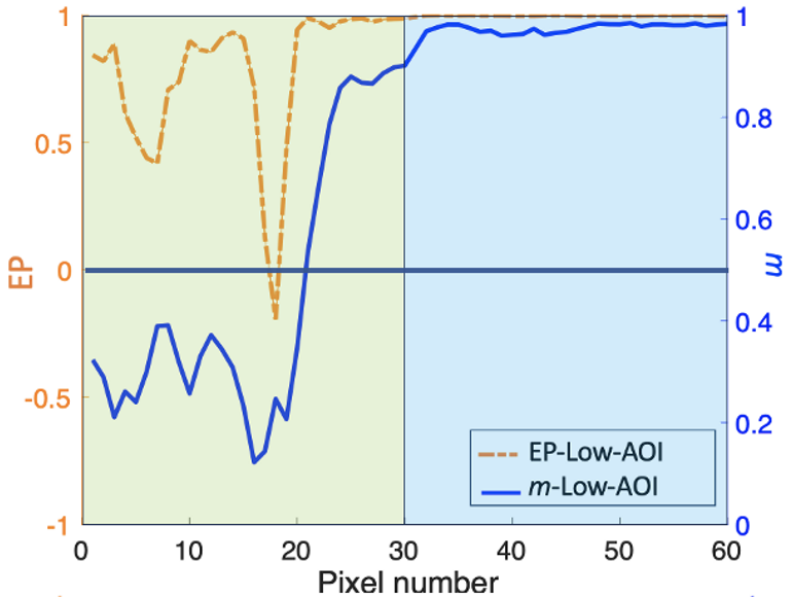

Figure 4.18 Plots of m and EP along the transect for case study 1 in Fig. 4.13. The green-shaded area indicates the vegetated region, while the blue-shaded area corresponds to the open water.

Table 4.5 EP and its (EP_std) for water and vegetation under low- and high-AOI conditions across four case studies. Each value was computed from 2,322 pixels.

Case	Water – Low AOI		Water – High AOI		Vegetation – Low AOI		Vegetation – High AOI	
	EP	EP_std	EP	EP_std	EP	EP_std	EP	EP_std
1	0.9979	0.0014	0.8429	0.0839	0.6717	0.2456	0.5229	0.3015
2	0.9954	0.0032	0.7829	0.1446	0.7200	0.2078	0.4716	0.3499
3	0.9794	0.0073	0.8960	0.0387	0.7710	0.1926	0.6703	0.2258
4	0.9829	0.0091	0.8966	0.0454	0.6067	0.2665	0.3607	0.3540

consistent with the findings obtained for case study 1, confirming that land–water contrast is more pronounced under high angle of incidence (AOI) conditions and decreases at lower AOI. As in the previous case, ancillary wind data were examined to assess environmental effects. For the acquisition on 1 July 2023 (panels a–b) at 01:04 UTC, the recorded wind speed was approximately 10 km/h at 01:00 UTC, corresponding to a time difference of only 4 minutes. For the 16 May acquisition (panels c–d), wind speeds ranged between 18 and 20 km/h from 00:00 to 01:00 UTC, with a maximum temporal offset of 12 minutes from the SAR acquisition time. The nearest meteorological station is located approximately 43 km from the study area. The overall analysis of the available wind records indicates comparable low-to-moderate wind conditions for both dates, supporting the conclusion that the observed differences in backscatter are primarily driven by radar geometry rather than atmospheric forcing.

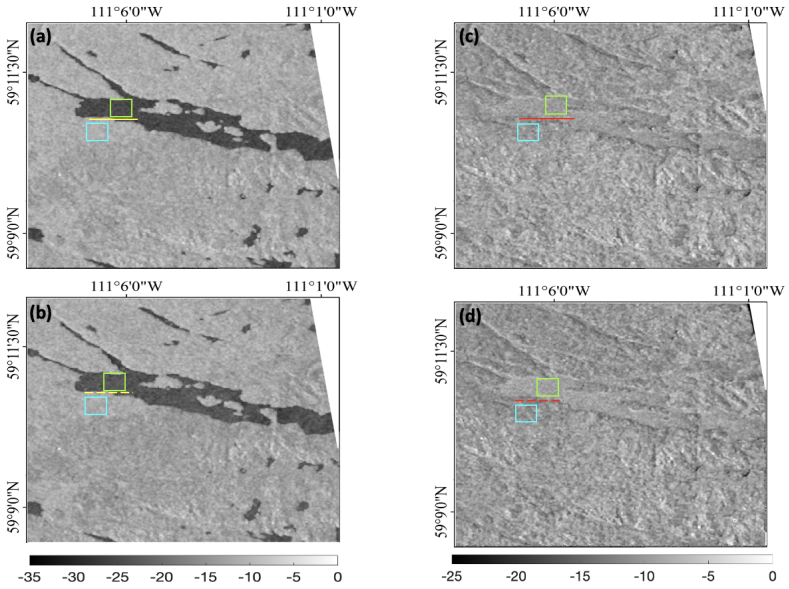

Figure 4.19 NRCS RCM HP images for case study 2. Panels (a) and (b) show the RH and RV channels acquired at high AOI, respectively, while panels (c) and (d) present the RH and RV channels acquired at low AOI. All images are displayed in grayscale using a decibel (dB) scale.

The polarimetric features demonstrate a clear improvement under low-AOI conditions, which is of both theoretical and practical relevance (see Fig. 4.20). In addition, basic polarimetric indicators were examined to verify the consistency of Case 2 with Case 1. EP and its (EP_std), illustrated in Fig.4.20, follow trends consistent with those reported in Table 4.5. Specifically, higher polarimetric stability is observed over water and greater variability over vegetation, particularly under low-AOI conditions. These results further confirm that polarimetric features enhance waterline discrimination, even in cases where NRCS contrast is limited.

In summary, these experiments suggest that proper polarimetric features can be particular relevant in the case of low contrast NRCS SAR HP images.

B. Sandy Coasts

The figure format for the NRCS images is identical to that used in the previous figures (see Fig. 4.21 and Fig. 4.22). The subjective analysis of these images clearly shows that the high AOI is better than the low AOI but now the contrast is not negligible even in the low AOI cases.

With respect to case 3, external acquisition refer to 3 june 2023, see Fig. 4.21 (a-b), at 01:04 UTC time, the wind speed is about 15 km/h, about 4.17 m/s, at 01:00 UTC time with 4 minutes difference. On 9 june, see Fig. 4.21 (c-d), wind speeds ranged

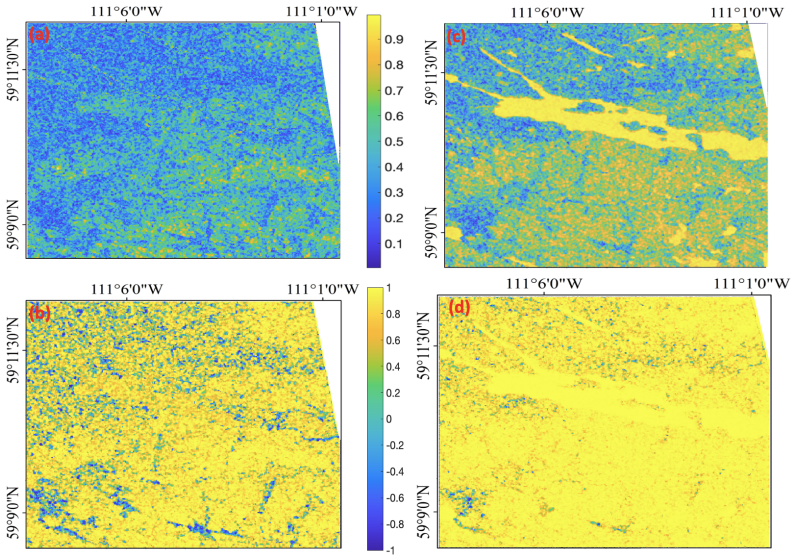

Figure 4.20 Polarimetric features maps relevant to case 2. On the left (right) column the High (Low) AOI are considered. In (a) and (c) m is shown, in (b) and (d) the EP.

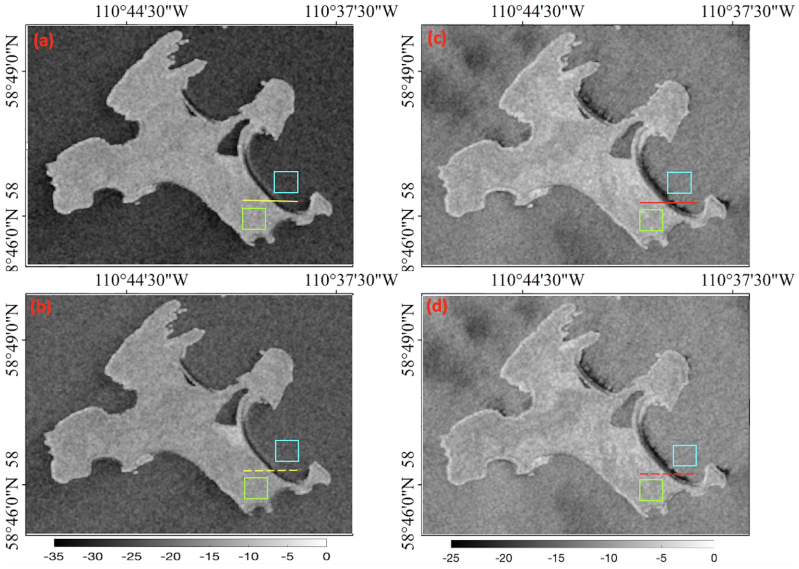

Figure 4.21 NRCS RCM HP images for case study 3. Panels (a) and (b) show the RH and RV channels acquired at high AOI, respectively, while panels (c) and (d) present the RH and RV channels acquired at low AOI. All images are displayed in grayscale using a decibel (dB) scale.

between 8–11 km/h from 00:00 to 01:00 UTC time, corresponding to a maximum time difference of 12 minutes. No rain is present. In this cases the weather station is about 30 km away. Analyzing all independent wind information we can reasonably state that wind follows low to moderate regimes.

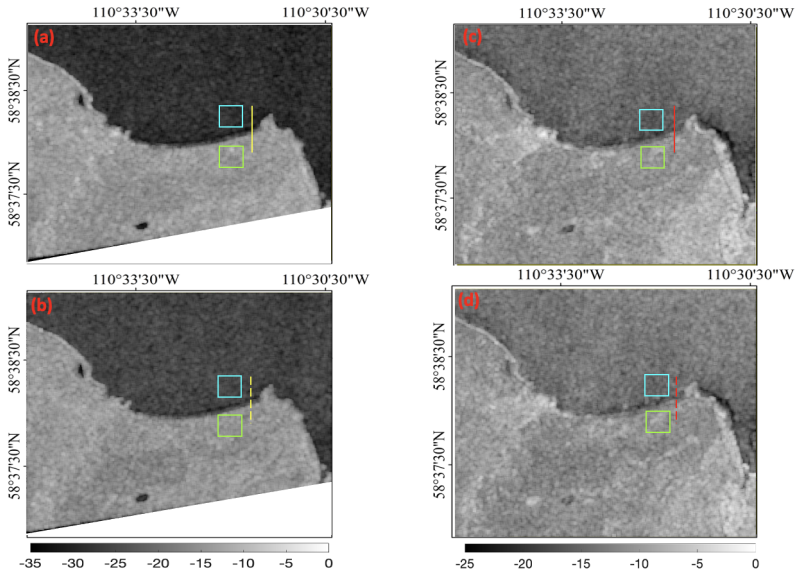

Figure 4.22 NRCS RCM HP images for case study 4. Panels (a) and (b) show the RH and RV channels acquired at high AOI, respectively, while panels (c) and (d) present the RH and RV channels acquired at low AOI. All images are displayed in grayscale using a decibel (dB) scale.

With reference to case 4 acquisitions refer to 3 june 2023, see Fig. 4.22(a-b), at 01:04 UTC time, the wind speed was 15 km/h, at 01:00 UTC time with 4 minutes difference. On 28 may, see Fig. 4.22 (c-d), wind speeds ranged between 14–18 km/h from 00:00 to 01:00 UTC time, corresponding to a maximum time difference of 12 minutes. No rain is present. In this case the weather station was about 37 km away. In this case, low to moderate wind regime is in place.

In addition to the NRCS analysis, the corresponding polarimetric features were also evaluated (see Fig. 4.23 and Fig. 4.24). Although a detailed polarimetric study is beyond the scope of this section, the m and EP maps provide valuable qualitative insights. The waterlines appear more distinct in terms of contrast, particularly under low-AOI conditions, supporting the general trends observed in the vegetated cases.

Quantitatively, the EP and its (EP_std) for these sandy cases follow the same pattern as summarized in Table 4.5. Higher EP values and lower EP_std are consistently observed over water surfaces, while sandy and land areas show greater variability. This confirms that, even in coastal environments with complex scattering, the polarimetric indicators maintain their ability to distinguish between surface types.

To provide a quantitative measure of the separability achieved by each polarimetric parameter, a statistical comparison was conducted using the Bhattacharyya distance. Table 4.6 summarizes the Bhattacharyya distances values for the four polarimetric

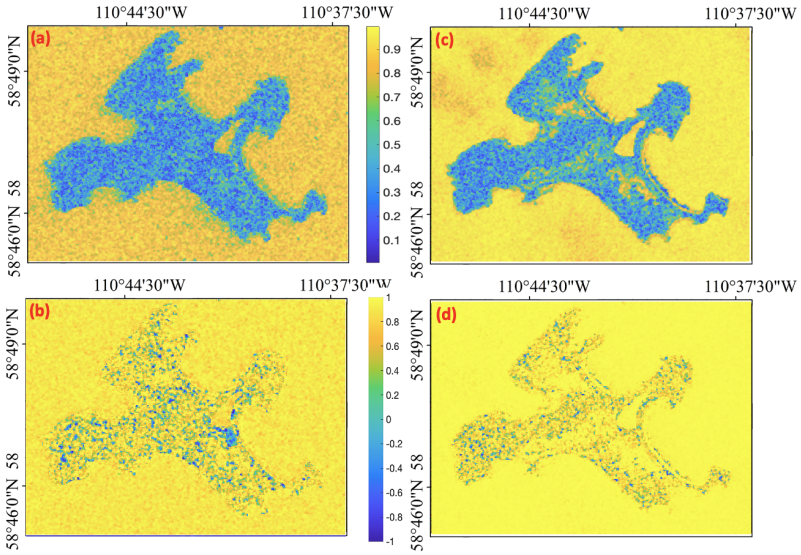

Figure 4.23 Polarimetric features maps relevant to case 3. On the left (right) column the High (Low) AOI are considered. In (a) and (c) m is shown, in (b) and (d) the EP.

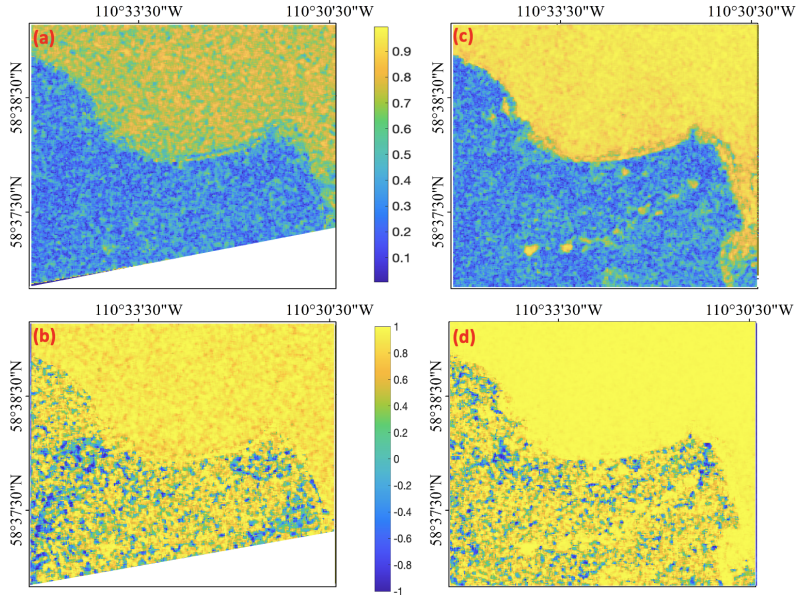

Figure 4.24 Polarimetric features maps relevant to case 4. On the left (right) column the High (Low) AOI are considered. In (a) and (c) m is shown, in (b) and (d) the EP.

metrics (RH, RV, m, and EP) across the four case studies under both low and high AOI conditions. A larger Bhattacharyya distance indicates stronger class separability between land and water. Under low AOI, the m parameter consistently shows the highest separability (Bhattacharyya distances up to 12.35), followed by EP in some cases, while RH and RV generally yield very low Bhattacharyya distances values, indicating weak discrimination. In contrast, at high AOI the situation reverses: RH

and RV exhibit extremely high Bhattacharyya distances values (e.g., RH = 74.01, RV = 31.23), reflecting strong discrimination, whereas m and EP drop to very low values, indicating poor separability. These results highlight that the most effective discriminating metric strongly depends on the AOI, with m performing best under low AOI and RH/RV dominating under high AOI.

Table 4.6 Bhattacharyya distance (BD) for four polarimetric metrics under low and high AOI conditions. Larger BD values indicate greater class separability.

Case	**Low AOI**				**High AOI**			
	RH	RV	m	EP	RH	RV	m	EP
Case 1	0.49	0.81	12.35	2.24	74.01	23.95	0.60	0.30
Case 2	0.06	0.18	1.93	1.17	69.82	31.23	0.25	0.14
Case 3	4.26	1.88	1.19	0.19	50.18	11.60	2.11	0.24
Case 4	3.25	1.39	11.67	1.14	34.91	12.17	2.41	0.87

4.3.4 Conclusive Remarks

In this part of the study, the changing waterlines of several sub-Arctic lakes in Alberta were examined using HP SAR data from the RCM in 2023. Four sites were chosen to capture a range of conditions, including both vegetated and sandy shorelines observed under different radar viewing angles. To check and refine the results, Sentinel-2 RGB images and NDVI data were used to confirm the position of lake boundaries. Together, these datasets provided a detailed picture of how land and water interact across different surface types and observation geometries. The main findings are summarised below:

- **Incidence angle effect:** High AOI images provided strong contrast between water and land, especially along vegetated coasts, due to enhanced volume scattering in vegetation and reduced backscatter from smooth water. Low AOI cases were more challenging, with weaker class separations.
- **Role of polarimetric features:** The parameters m and EP markedly improved discrimination in low AOI conditions, particularly for vegetated waterlines. Bhattacharyya distance analysis showed that m achieved the highest separability at low AOI, while RH and RV dominated at high AOI.
- **Vegetated vs. sandy coasts:** Vegetated shorelines benefited most from polarimetric features, whereas sandy shorelines showed weaker but still measurable

improvements. Narrow sandy zones posed challenges due to mixed scattering within a single SAR resolution cell.

- **Quantitative performance:** Under high AOI, RH and RV achieved very strong separability (e.g., RH = 74.01 in Case 1), whereas under low AOI, m reached values up to 12.35, outperforming amplitude-only metrics.

Significance and alignment with aims. The results presented in this section address the main goals of this dissertation, particularly the second and third research aims introduced in Chapter 1. The focus here is on detecting and outlining waterlines, rather than tracking long-term temporal changes. Even so, the findings contribute to the broader monitoring objective by showing that CP SAR data can improve the accuracy and interpretation of boundary detection. In addition, the analysis of the polarimetric parameters m and EP supports the third aim by providing useful information about how scattering behaviour varies with surface type and imaging geometry. When viewed together with the Antarctic and glacier case studies, these results highlight the value of polarimetric SAR for studying cryospheric and hydrological boundaries in Canada.

Outlook. The results show that CP features can be used effectively to monitor waterlines in sub-Arctic lakes. More testing with longer data records is needed to assess how stable these features are during flooding, ice cover, and other strong weather events. Using the same approach across other northern lakes would help determine whether the patterns observed here also occur elsewhere and how local shoreline changes connect to broader hydrological and climatic effects.

Chapter 5

Conclusion and Future Work

5.1 Conclusions

This dissertation examined how polarimetric and multi-polarisation SAR data can be used to monitor cryospheric and hydrological boundaries. Detecting the edges of ice fronts, icebergs, and lake shorelines remains a challenging task, especially in polar and sub-Arctic regions where frozen seas, vegetation, and sandy coasts all influence radar backscatter. PolSAR however, offers additional information beyond single-pol images, allowing a more physical interpretation of scattering and boundary behaviour.

The research focused on how polarisation and imaging geometry affect scattering and the ability of C-band SAR to detect and track boundaries under different conditions. The analysis was organised around four main case studies:

1. The short- and long-term dynamics of the DIT in East Antarctica using Sentinel-1 data;

2. The drift and scattering behaviour of the C33 iceberg in Terra Nova Bay, using Sentinel-1 dual-pol observations;

3. The temporal evolution of the d'Iberville Glacier front on Ellesmere Island (Nunavut) from 2010 to 2022, analysed with Radarsat-2 and Sentinel-1 data; and

4. The detection of shorelines in sub-Arctic lakes in Alberta, based on RCM CP imagery.

Together, these case studies form a consistent framework for evaluating how polarimetric SAR performs across very different environments, from Antarctic glaciers and icebergs to northern Canadian lakes.

5.1.1 Key Findings

For the DIT, advance rates averaged around 670 m/year (typically 600–800 m/year), confirming its ongoing instability and matching previous C-band studies. Turning to the C33 iceberg, the cross-polarised HV channel provided the clearest boundary contrast, while parameters derived from the covariance matrix, especially the DoP, helped describe how scattering evolved during its 67 km drift.

For the d'Iberville Glacier the front retreated at an average rate of roughly 160 m/year between 2010 and 2022, though with significant year-to-year variability, from about 514 m/year in 2010–2011 to near stability in 2021–2022. The total surface loss was around 2.2 km^2.

In the RCM lake analysis, incidence angle emerged as the dominant control. High AOI (38–42°) improved contrast over vegetated coasts by enhancing volume scattering, whereas low AOI (20–24°) reduced this contrast. Under such low-angle conditions, compact polarimetric parameters such as the Degree of Polarisation (m) and EP became more effective for detecting complex or mixed shorelines.

Across all studies, two factors consistently governed boundary detection: **(i)** imaging geometry, particularly the incidence angle, and **(ii)** the inclusion of polarimetric information (dual-pol or CP). Together, these determine how clearly and reliably boundaries can be identified in SAR imagery.

5.1.2 Limitations

The results reflect the specific setup of C-band sensors, viewing geometry, and processing parameters used in this research (e.g., multilooking, CFAR thresholds, terrain correction). Optical reference images were typically acquired within ±3 days of the SAR data, so some differences in shoreline position may result from tidal variation or short-term changes in water level. The 16 m spatial resolution of RCM also means that narrow beaches or transition zones may fall within a single pixel, reducing spatial precision. Nevertheless, the land–water contrasts were generally stable and only weakly affected by noise or short-term wind effects.

5.1.3 Synthesis and Significance

Overall, this work shows that polarimetric SAR can be applied systematically to monitor cryospheric and hydrological boundaries. By linking imaging geometry and polarisation type to detection quality, it provides a basis for developing monitoring methods that adapt to changing environmental and viewing conditions.

From an operational perspective, several practical guidelines can be drawn:

- **High AOI (38–42°):** RH and RV (NRCS) channels work best for vegetated shorelines;
- **Low AOI (20–24°):** compact polarimetric parameters (m, EP) are preferred when NRCS contrast is limited;
- **Sea-ice and iceberg zones:** HV or DoP-based features enhance edge visibility.

These results highlight how combining geometric configuration with polarimetric information improves both the scientific understanding and operational monitoring of rapidly changing northern and polar environments.

5.2 Future Developments

The findings of this dissertation open several directions for further investigation and refinement of polarimetric SAR applications in cryospheric and hydrological studies:

1. **Higher-resolution RCM analysis:** Future work should take advantage of the newer high-resolution imaging modes of the RCM such as Spotlight and Fine Quad. These modes, with pixel spacing below 5 m, can resolve narrow beaches, thin ice margins, and vegetated shorelines that were only partly captured in the present analysis. Studying how spatial resolution affects the behaviour of polarimetric parameters such as m and EP would help to improve boundary delineation in mixed land–water areas.
2. **Thickness estimation using L-band SAR:** Extending the study to longer wavelengths, such as L-band data from the NISAR mission, would provide valuable information about ice and snow thickness. The increased penetration depth at L-band enhances sensitivity to subsurface and volume scattering. Combining L-band polarimetric parameters with coherence or backscatter attenuation could support the development of empirical approaches for estimating thickness in glacier and lake environments.
3. **Regional and temporal extension:** The methods developed here could be applied to additional glaciers, icebergs, and lakes across both hemispheres to test their consistency under different environmental conditions. A longer time series would also allow assessment of the temporal stability of compact-polarimetric parameters during seasonal transitions such as freeze, melt, and flood events.

4. **Climatic integration:** Relating SAR-derived boundary changes to environmental variables such as air temperature, wind speed, precipitation, and river discharge would clarify the processes driving the observed surface variability. Integrating these factors would enhance the physical interpretation of SAR observations within a broader climatic context.

5. **Next-generation sensors:** Applying the same analytical framework to upcoming missions—including, NISAR (L-band), and BIOMASS (P-band)—will extend the available spectral range and enhance the monitoring of regions affected by volume scattering, surface roughness, and complex terrain geometry.

6. **Automated and adaptive processing:** Developing algorithms that automatically identify the most suitable polarimetric features for specific incidence angles and surface types would enable near-real-time monitoring and operational use of CP SAR data.

7. **Uncertainty assessment:** Future analyses should include a quantitative evaluation of accuracy using confidence intervals for RMSE, contrast, and Bhattacharyya distance. Establishing these error estimates will ensure comparability between different sensors and study regions.

8. **Multi-frequency comparison:** Finally, examining whether the relationships between NRCS, DoP, and EP observed at C-band also hold at other frequencies, including shorter wavelengths such as X-band and longer wavelengths such as L- or P-band, would help to generalise the findings and provide a more comprehensive understanding of wavelength-dependent scattering mechanisms across both surface- and volume-dominated regimes.

Short CV and list of publications

Mozhgan Zahriban Hesari was born in Gorgan, Iran, on 5 July 1989.
In 2013, she received her Master's Degree in Natural Resources from the University of Sari, iran, where her thesis focused on estimating forest structural characteristics using Pleiades satellite data and auxiliary environmental information. From 2014 to 2020, she conducted research on forest parameter estimation using TanDEM-X SAR data, applying InSAR techniques and regression modeling to derive canopy height and assess forest structure in the Hyrcanian ecosystems at Gorgan University of Agricultural Sciences and Natural Resources, in collaboration with the Swedish University of Agricultural Sciences (Umeå, Sweden).
From 2021 to 2022, she was awarded a research grant at the University of Naples "Parthenope," where she worked on multi-polarisation SAR measurements for cryospheric observation. Since November 2022, she has been a Ph.D. candidate in Information and Communication Technology and Engineering (XXXVIII cycle) at the University of Naples "Parthenope," within the curriculum of Applied Electromagnetics. Her research interests include polarimetric SAR processing, electromagnetic scattering modelling, and environmental remote sensing applications for cryospheric and coastal monitoring.
She is the author or co-author of scientific papers published in international peer-reviewed journals, including *IEEE Journal of Oceanic Engineering*, *Remote Sensing*, *International Journal of Remote Sensing*, and *Canadian Journal of Remote Sensing*, as well as several international conference proceedings (IEEE IGARSS, MetroSea, and Living Planet Symposium).
She serves as a reviewer for IEEE and Taylor & Francis journals and is a student member of the Institute of Electrical and Electronics Engineers (IEEE), the Geoscience and Remote Sensing Society (GRSS), and the Oceanic Engineering Society (OES).

Visiting Scientist

April–July 2025 — Department of Earth Observation Science (EOS), University of Twente, The Netherlands.Polarimetric SAR decomposition for iceberg characterization.

Peer-Reviewed Journal Papers

1. A. Buono, F. Nunziata, M. Z. Hesari, G. Aulicino, G. Fusco, and M. Migliaccio, "On the exploitation of dual-polarimetric SAR measurements to observe the C33 iceberg in Antarctica," *IEEE Journal of Oceanic Engineering*, vol. 50, no. 2, pp. 537–548, IEEE, 2025.

2. M. Zahriban Hesari, A. Buono, F. Nunziata, G. Aulicino, and M. Migliaccio, "Multi-Polarisation C-Band SAR Imagery to Estimate the Recent Dynamics of the d'Iberville Glacier," *Remote Sensing*, vol. 14, p. 5758, MDPI, 2022.

3. M. Zahriban Hesari, F. Nunziata, G. Aulicino, A. Buono, and M. Migliaccio, "Analysis of fine-scale dynamics of the Drygalski Ice Tongue in Antarctica using satellite SAR data," *International Journal of Remote Sensing*, vol. 43, no. 7, pp. 2581–2598, Taylor & Francis, 2022.

Refereed Conference Papers

1. Z. Khan, M. Zahribanhesari, F. Nunziata, D. Gleich, P. Planinšič, and M. Migliaccio, "SAR-Driven Time Variability Analysis of the Coastline of the Lake Ptuj, Slovenia," in *Proc. 2024 IEEE International Workshop on Metrology for the Sea (MetroSea)*, pp. 100–104, IEEE, 2024.

2. M. Zahribanhesari, F. Nunziata, M. Migliaccio, and M. Dabboor, "Dual-Polarimetric SAR Imaging Modes to Monitor Lake Extent," in *Proc. 2024 IEEE International Geoscience and Remote Sensing Symposium (IGARSS)*, pp. 673–676, IEEE, 2024.

3. M. Migliaccio, M. Zahribanhesari, A. Buono, S. Cappa and M. Dabboor, "On the Observation of Water Bodies by Means of Compact Polarimetric Synthetic Aperture Radar Imagery," in *OCEANS 2024* pp. 1–5, OCEANS 2024 - Singapore.

4. M. Z. Hesari, G. Inserra, G. Aulicino, and M. Migliaccio, "A Spatio-Temporal Variability Assessment of the C33 Iceberg Using Multi-Polarisation C-Band SAR Satellite Data," in *Proc. 2023 IEEE International Workshop on Metrology for the Sea (MetroSea)*, pp. 395–399, IEEE, 2023.

5. M. Z. Hesari, A. Buono, G. Aulicino, and M. Migliaccio, "On the Time Evolution of the d'Iberville Glacier Using C-Band SAR Data," in *Proc. 2022 IEEE International Workshop on Metrology for the Sea (MetroSea)*, pp. 419–423, IEEE, 2022.

Bibliography

[1] A. Moreira, C. Prati, G. Krieger, J. Mittermayer, H. Fiedler, and I. Hajnsek, "A tutorial on synthetic aperture radar," *IEEE Geoscience and Remote Sensing Magazine*, vol. 1, no. 1, pp. 6–43, 2013.

[2] G. Aulicino, M. Sansiviero, S. Paul, C. Cesarano, G. Fusco, P. Wadhams, and G. Budillon, "A new approach for monitoring the terra nova bay polynya through modis ice surface temperature imagery and its validation during 2010 and 2011 winter seasons," *Remote Sensing*, vol. 10, no. 3, 2018.

[3] NASA Earth Observatory, "Antarctic ice shelf sheds bergs." https://earthobservatory.nasa.gov/images/87859/antarctic-ice-shelf-sheds-bergs, 2016. Accessed: 2025-09-20.

[4] Encyclopaedia Britannica Editors, "Antarctica." Encyclopaedia Britannica, 2025. Accessed: 2025-09-17.

[5] Antarctic and Southern Ocean Coalition, "Climate crisis in antarctica." ASOC, 2025. Accessed: 2025-09-17.

[6] British Antarctic Survey, "Antarctic factsheet: Geographical statistics." British Antarctic Survey, 2025. Accessed: 2025-09-17.

[7] O. of Technology Assessment, "Potential mineral resources in antarctica," Tech. Rep. OTA-ITE-542, U.S. Congress, 1989.

[8] IPCC, "Climate change 2021: The physical science basis," 2021. Contribution of Working Group I to the Sixth Assessment Report of the Intergovernmental Panel on Climate Change.

[9] T. Tin, Z. L. Fleming, K. A. Hughes, D. Ainley, P. Convey, C. Moreno, S. Pfeiffer, J. Scott, and I. Snape, "Impacts of local human activities on the antarctic environment," *Antarctic Science*, vol. 21, no. 1, pp. 3–33, 2009.

[10] National Snow and Ice Data Center, "Why arctic weather and climate matter." https://nsidc.org/learn/parts-cryosphere/arctic-weather-and-climate/why-arctic-weather-and-climate-matter, 2020. Accessed: 2025-09-23.

[11] T. D. Prowse, K. Alfredsen, S. Beltaos, B. R. Bonsal, C. R. Duguay, A. Korhola, J. McNamara, R. Pienitz, W. F. Vincent, V. Vuglinsky, and G. A. Weyhenmeyer, "Effects of changes in arctic lake and river ice," *Ambio*, vol. 40, no. Suppl 1, pp. 63–74, 2011.

[12] A. J. Cook, L. Copland, B. P. Y. Noel, C. R. Stokes, M. J. Bentley, M. J. Sharp, R. G. Bingham, T. Bolch, B. S. Case, B. J. Davies, S. S. R. Jamieson, R. Carr, E. Gilbert, A. Muir, and B. Wouters, "Accelerated retreat of canadian arctic glaciers since the early 2000s," *Geophysical Research Letters*, vol. 46, no. 1, pp. 653–662, 2019.

[13] H. P. Huntington, J. Olsen, E. Zdor, A. Zagorskiy, H. C. Shin, O. Romanenko, B. Kaltenborn, J. Dawson, J. Davies, and E. Abou-Abbsi, "Effects of arctic commercial shipping on environments and communities: context, governance, priorities," *Transportation Research Part D: Transport and Environment*, vol. 118, p. 103731, 2023.

[14] X. Qi, Z. Li, C. Zhao, Q. Zhang, and Y. Zhou, "Environmental impacts of arctic shipping activities: A review," *Ocean & Coastal Management*, vol. 247, p. 106936, 2024.

[15] T. Løken, J. Rabault, A. Jensen, G. Sutherland, K. H. Christensen, and M. Müller, "Wave measurements from ship mounted sensors in the arctic marginal ice zone (miz)," *arXiv preprint arXiv:1911.07612*, 2019.

[16] J. A. Maslanik and R. G. Barry, "Remote sensing in antarctica and the southern ocean: applications and developments," *Antarctic science*, vol. 2, no. 2, pp. 105–121, 1990.

[17] Y. Li, G. Qiao, S. Popov, X. Cui, I. V. Florinsky, X. Yuan, and L. Wang, "Unmanned aerial vehicle remote sensing for antarctic research: A review of progress, current applications, and future use cases," *IEEE Geoscience and Remote Sensing Magazine*, vol. 11, no. 1, pp. 73–93, 2023.

[18] N. Zakhvatkina, V. Smirnov, and I. Bychkova, "Satellite sar data-based sea ice classification: An overview," *Geosciences*, vol. 9, no. 4, p. 152, 2019.

[19] Y. K. Chan and V. Koo, "An introduction to synthetic aperture radar (sar)," *Progress In Electromagnetics Research B*, vol. 2, pp. 27–60, 2008.

[20] G. Inserra, A. Buono, F. Nunziata, M. Migliaccio, F. Parmiggiani, and G. Aulicino, "Characterization of the terra nova bay polynya using dual-polarimetric c-band sar measurements," *IEEE Journal of Oceanic Engineering*, vol. 49, no. 3, pp. 856–869, 2024.

[21] M. Zahriban Hesari, A. Buono, F. Nunziata, G. Aulicino, and M. Migliaccio, "Multi-polarisation c-band sar imagery to estimate the recent dynamics of the d'iberville glacier," *Remote Sensing*, vol. 14, no. 22, p. 5758, 2022.

[22] A. Buono, F. Nunziata, M. Z. Hesari, G. Aulicino, G. Fusco, and M. Migliaccio, "On the exploitation of dual-polarimetric sar measurements to observe the c33 iceberg in antarctica," *IEEE Journal of Oceanic Engineering*, 2025.

[23] J.-S. Lee and E. Pottier, *Polarimetric Radar Imaging: From Basics to Applications*. CRC Press, 2009.

[24] A. C. Frery, H. J. Müller, C. D. Yanasse, and S. J. S. Sant'Anna, "A model for extremely heterogeneous clutter," *IEEE Transactions on Geoscience and Remote Sensing*, vol. 35, no. 3, pp. 648–659, 1997.

[25] C. A. Wiley, "Synthetic aperture radar," *Proceedings of the IRE*, vol. 39, no. 10, pp. 1636–1636, 1951.

[26] F. M. Henderson and A. J. Lewis, *Principles and Applications of Imaging Radar*. Manual of Remote Sensing, Vol. 2, John Wiley & Sons, 1998.

[27] J. W. Goodman, "Some fundamental properties of speckle," *JOSA*, vol. 66, no. 11, pp. 1145–1150, 1976.

[28] S. R. Cloude, *Polarisation: Applications in Remote Sensing*. Oxford University Press, 2007.

[29] R. K. Raney, "Hybrid-polarity sar architecture," *IEEE Transactions on Geoscience and Remote Sensing*, vol. 45, no. 11, pp. 3397–3404, 2007.

[30] A. Buono, A. Nunziata, and M. Migliaccio, "A new methodology to detect icebergs using polarimetric sar imagery," *IEEE Journal of Selected Topics in Applied Earth Observations and Remote Sensing*, vol. 9, no. 4, pp. 1423–1432, 2016.

[31] E. Ferrentino, A. Buono, F. Nunziata, A. Marino, and M. Migliaccio, "On the use of multipolarization satellite sar data for coastline extraction in harsh coastal environments: The case of solway firth," *IEEE Journal of Selected Topics in Applied Earth Observations and Remote Sensing*, vol. 14, pp. 249–257, 2020.

[32] E. Ferrentino, F. Nunziata, A. Buono, A. Urciuoli, and M. Migliaccio, "Multipolarization time series of sentinel-1 sar imagery to analyze variations of reservoirs' water body," *IEEE Journal of Selected Topics in Applied Earth Observations and Remote Sensing*, vol. 13, pp. 840–846, 2020.

[33] S. R. Cloude, "Dual-polarisation coherence and degree of polarisation," *IEEE Geoscience and Remote Sensing Letters*, vol. 11, no. 6, pp. 1160–1164, 2014.

[34] R. K. Raney, R. D. D. Henry, R. M. Beal, and R. C. Jordan, "The hybrid-polarimetric architecture for spaceborne sar," *IEEE Transactions on Geoscience and Remote Sensing*, vol. 49, no. 10, pp. 3532–3543, 2011.

[35] R. K. Raney, "Hybrid-polarity sar architecture," *IEEE Transactions on Geoscience and Remote Sensing*, vol. 45, no. 11, pp. 3397–3404, 2007.

[36] R. K. Raney, "A perspective on compact polarimetry in radar remote sensing," *IEEE Geoscience and Remote Sensing Letters*, vol. 8, no. 5, pp. 973–976, 2011.

[37] J.-C. Souyris, P. Imbo, R. Fjørtoft, S. Mingot, and J. S. Lee, "Compact polarimetry: A new concept for high-resolution sar," *IEEE Transactions on Geoscience and Remote Sensing*, vol. 43, no. 3, pp. 634–646, 2005.

[38] M. Born and E. Wolf, *Principles of Optics*. Pergamon Press, 6th ed., 1980.

[39] A. Nunziata and M. Migliaccio, "On the polarimetric properties of sea and land surfaces: An application to compact polarimetry," *IEEE Journal of Selected Topics in Applied Earth Observations and Remote Sensing*, vol. 7, no. 7, pp. 2781–2788, 2014.

[40] C. Stevens, W. S. Lee, G. Fusco, S. Yun, B. Grant, N. Robinson, and C. Y. Hwang, "The influence of the drygalski ice tongue on the local ocean," *Annals of Glaciology*, vol. 58, no. 74, pp. 51–59, 2017.

[41] M. Frezzotti and M. C. Mabin, "20th century behaviour of drygalski ice tongue, ross sea, antarctica," *Annals of Glaciology*, vol. 20, pp. 397–400, 1994.

[42] G. Holdsworth, "Some effects of ocean currents and wave motion on the dynamics of floating glacier tongues," *Oceanology of the Antarctic continental shelf*, vol. 43, pp. 253–271, 1985.

[43] F. Parmiggiani and C. Fragiacomo, "The calving event of the drygalski ice tongue of february 2005," *International Journal of Remote Sensing*, vol. 26, no. 21, pp. 4633–4638, 2005.

[44] J. Wuite, K. Jezek, X. Wu, K. Farness, and R. Carande, "The velocity field and flow regime of david glacier and drygalski ice tongue, antarctica," *Polar Geography*, vol. 32, no. 3-4, pp. 111–127, 2009.

[45] A. Buono, F. Nunziata, L. Mascolo, and M. Migliaccio, "A multipolarization analysis of coastline extraction using x-band cosmo-skymed sar data," *IEEE Journal of Selected Topics in Applied Earth Observations and Remote Sensing*, vol. 7, no. 7, pp. 2811–2820, 2014.

[46] S. Sayama and S. Ishii, "Suppression of log-normal distributed weather clutter observed by an s-band radar," *Wireless Engineering and Technology*, vol. 3, no. 3, pp. 12–133, 2013.

[47] H. Liu and K. C. Jezek, "Automated extraction of coastline from satellite imagery by integrating canny edge detection and locally adaptive thresholding methods," *International journal of remote sensing*, vol. 25, no. 5, pp. 937–958, 2004.

[48] C.-S. Lee, N. Seo, K.-S. Seo, T. A. Scambos, and R. Ross, "Transverse motion of drygalski ice tongue, antarctica correlated with thermohaline circulations in terra nova bay polynya," in *AGU Fall Meeting Abstracts*, vol. 2013, pp. C21A–0624, 2013.

[49] NASA, "Antarctica's drygalski ice tongue," *Dataset accessed [2021-10-10] at http://landsat.gsfc.nasa.gov/sites/landsat/files/2012/12/landsat_drygalski_vf_4web*, 2012.

[50] Z. Chen, X. Cheng, and F. Hui, "Changes monitoring of the drygalski ice tongue front during 1973 to 2012," in *EGU General Assembly Conference Abstracts*, p. 270, 2014.

[51] C. Indrigo, C. F. Dow, J. Greenbaum, and M. Morlighem, "Drygalski ice tongue stability influenced by rift formation and ice morphology," *Journal of Glaciology*, vol. 67, no. 262, pp. 243–252, 2021.

[52] C. Indrigo, "The stability of the drygalski ice tongue," Master's thesis, University of Waterloo, 2019.

[53] M. Zahriban Hesari, F. Nunziata, G. Aulicino, A. Buono, and M. Migliaccio, "Analysis of fine-scale dynamics of the drygalski ice tongue in antarctica using satellite sar data," *International Journal of Remote Sensing*, vol. 43, no. 7, pp. 2581–2598, 2022.

[54] T. Li, Y. Ding, T. Zhao, and X. Cheng, "Iceberg calving from the antarctic nansen ice shelf in april 2016 and its local impact," *Science Bulletin*, vol. 61, no. 15, pp. 1157–1159, 2016.

[55] S. Vallender, "Calculation of the wasserstein distance between probability distributions on the line," *Theory of Probability & Its Applications*, vol. 18, no. 4, pp. 784–786, 1974.

[56] E. Ferrentino, C. Bignami, F. Nunziata, S. Stramondo, and M. Migliaccio, "On the ability of dual-polarimetric sar measurements to observe lava flows under different volcanic environments," *International Journal of Applied Earth Observation and Geoinformation*, vol. 123, p. 103471, 2023.

[57] M. A. Richards *et al.*, *Fundamentals of radar signal processing*, vol. 1. Mcgraw-hill New York, 2005.

[58] G. V. Weinberg and C. Tran, "Burr distribution for x-band maritime surveillance radar clutter," *Progress In Electromagnetics Research B*, vol. 81, pp. 183–201, 2018.

[59] M. Moctezuma-Flores and F. Parmiggiani, "Tracking of the iceberg created by the nansen ice shelf collapse," *International Journal of Remote Sensing*, vol. 38, no. 5, pp. 1224–1234, 2017.

[60] World Bank, Climate Change Knowledge Portal, "Climate-data historical for greenland." https://climateknowledgeportal.worldbank.org/country/greenland/climate-data-historical, 2022. Accessed: 29 August 2022.

[61] C. A. Baumhoer, A. J. Dietz, C. Kneisel, and C. Kuenzer, "Automated extraction of antarctic glacier and ice shelf fronts from sentinel-1 imagery using deep learning," *Remote Sensing*, vol. 11, no. 21, p. 2529, 2019.

[62] F. Holdsworth, "Ice flow and related measurements of d'iberville glacier, ellesmere island, n.w.t., canada," unpublished manuscript, [Institution if known], [City, Province/Territory if known], 1977. Ellesmere Island, Northwest Territories.

[63] R. Millan, J. Mouginot, and E. Rignot, "Mass budget of the glaciers and ice caps of the queen elizabeth islands, canada, from 1991 to 2015," *Environmental Research Letters*, vol. 12, no. 2, p. 024016, 2017.

[64] N. Short and A. Gray, "Glacier dynamics in the canadian high arctic from radarsat-1 speckle tracking," *Canadian Journal of Remote Sensing*, vol. 31, no. 3, pp. 225–239, 2005.

[65] S. Williamson, M. Sharp, J. Dowdeswell, and T. Benham, "Iceberg calving rates from northern ellesmere island ice caps, canadian arctic, 1999–2003," *Journal of Glaciology*, vol. 54, no. 186, pp. 391–400, 2008.

[66] W. Van Wychen, J. Davis, D. O. Burgess, L. Copland, L. Gray, M. Sharp, and C. Mortimer, "Characterizing interannual variability of glacier dynamics and dynamic discharge (1999–2015) for the ice masses of ellesmere and axel heiberg islands, nunavut, canada," *Journal of Geophysical Research: Earth Surface*, vol. 121, no. 1, pp. 39–63, 2016.

[67] W. Kochtitzky and L. Copland, "Retreat of northern hemisphere marine-terminating glaciers, 2000–2020," *Geophysical Research Letters*, vol. 49, no. 3, p. e2021GL096501, 2022.

[68] Encyclopædia Britannica, "Lake athabasca." https://www.britannica.com/place/Lake-Athabasca, n.d.

[69] Wikipedia contributors, "Bustard island." https://en.wikipedia.org/wiki/Bustard_Island, n.d. Accessed: 2025-05-06.

[70] Angler's Atlas, "Ryan lake." https://www.anglersatlas.com/place/102034/ryan-lake, n.d. Accessed: 2025-05-06.

[71] M. Dabboor, B. Montpetit, and S. Howell, "Assessment of the high resolution sar mode of the radarsat constellation mission for first year ice and multiyear ice characterization," *Remote Sensing*, vol. 10, no. 4, p. 594, 2018.

[72] L. White, K. Millard, S. Banks, M. Richardson, J. Pasher, and J. Duffe, "Moving to the radarsat constellation mission: Comparing synthesized compact polarimetry and dual polarimetry data with fully polarimetric radarsat-2 data for image classification of peatlands," *Remote Sensing*, vol. 9, no. 6, p. 573, 2017.